MONTANUNIVERSITÄT LEOBEN

Structural investigations on TiAlN coatings alloyed with C

Diploma Thesis

by

Fabian Konstantiniuk

This work has been carried out at the Chair of Functional Materials and Material Systems, Montanuniversitat Leoben, Austria

Leoben, September 2017

Affidavit

I declare in lieu of oath, that I wrote this thesis and performed the associated research myself, using only literature cited in this volume.

Leoben, June 2017

Fabian Konstantiniuk

Acknowledgments

I would like to thank Univ. Prof. DI Dr.mont. Christian Mitterer, head of the Chair of Function Materials and Material Systems, for giving me the opportunity to write this thesis and his professional supervision.

I am very grateful to my supervisor DI Dr.mont. Michael Tkadletz for his advice, his patience while answering all my questions and for the thorough read troughs and corrections of the manuscript.

Sincere thanks to all members of the Thin Films Group for the great support whenever needed and the pleasurable working atmosphere. Special thanks go to Mag. Velislava Terziyska and Dipl.-Ing. Anna Hofer for their support and their help at any time.

Financial support by the Austrian Federal Government (in particular from Bundesministerium für Verkehr, Innovation und Technologie and Bundesministerium für Wissenschaft, Forschung und Wirtschaft) represented by Österreichische Forschungsförderungsgesellschaft mbH and the Styrian and the Tyrolean Provincial Government, represented by Steirische Wirtschaftsförderungsgesellschaft mbH and Standortagentur Tirol, within the framework of the COMET Funding Programme is gratefully acknowledged.

Finally, I am grateful to my family, my friend and colleagues. Without their help and pursuing my studies would have been much more effort.

Abstract

TiAlN based hard coatings are widely applied on surfaces for cutting and forming tools because of their outstanding mechanical properties and oxidation resistance. Due to the steadily increasing demands on these coatings, the development of new alloy concepts is the focus of numerous scientific studies. In this work, the improvement of TiAlN coatings by alloying with carbon was investigated. A series of TiAlNC coatings with various C contents was synthesized by magnetron co-sputtering of Ti/Al und C targets in a mixed Ar-N_2 atmosphere using deposition temperatures of 25 and 500 °C, respectively. The elemental composition of the coatings was analyzed by energy-dispersive X-ray spectroscopy, the microstructure by X-ray diffraction and the chemical bonding states by X-ray photoelectron spectroscopy and Raman spectroscopy. Furthermore, nanoindentation was used to characterize hardness and Young´s modulus of the coatings, while the electrical resistivity was measured by the four-point probe method. It was found that the C content and the deposition temperature have a significant effect on the microstructure and the mechanical and electrical properties of TiAlNC coatings. A microstructure evolution from crystalline TiAlN to amorphous TiAlNC was observed with increasing C content. Furthermore, the hardness of TiAlN coatings can be increased by the addition of C. Another observation was that higher C contents in the coatings lead to an increase of the electrical resistivity. These insights, found within this diploma thesis, may serve as a valuable basis for the further development of TiAlNC coatings.

Kurzfassung

TiAlN-basierte Hartstoffschichten werden aufgrund ihrer hervorragenden mechanischen Eigenschaften und Oxidationsbeständigkeit für Schneid- und Umformwerkzeuge verwendet. Wegen der stetig steigenden Anforderungen an die Beschichtungen wird die Entwicklung verbesserter Legierungskonzepte vorangetrieben. In dieser Arbeit liegt der Schwerpunkt auf der Verbesserung des TiAlN Schichtsystems durch Legieren mit Kohlenstoff. Eine Reihe von TiAlNC Beschichtungen mit unterschiedlichen C Gehalten wurde durch Magnetron Co-Sputtern von Ti/Al und C-Targets in einer Ar-N_2 Atmosphäre mit Beschichtungstemperaturen von 25 bzw. 500 °C hergestellt. Die chemische Zusammensetzung der Beschichtungen wurde mittels energiedispersiver Röntgenspektroskopie festgestellt, während die Mikrostruktur mittels Röntgendiffraktometrie untersucht wurde. Durch Röngtenphotoelektronenspektroskopie und Raman-Spektroskopie wurden die chemischen Bindungszustände detektiert. Die Härte und der Elastizitätsmodul der Beschichtungen wurde mit Hilfe der Nanoindentation untersucht, während der elektrische Widerstand mit der Vier-Punkt-Methode erforscht wurde. Es zeigte sich, dass der C Gehalt und die Beschichtungstemperatur einen signifikanten Einfluss auf die Mikrostruktur und die mechanischen und elektrischen Eigenschaften der TiAlNC Schichten haben. Mit zunehmendem C Gehalt konnte eine Veränderung der Mikrostruktur von kristallinem TiAlN zu amorphem TiAlNC beobachtet werden. Des Weiteren zeigte sich, dass ein erhöhter C Gehalt zu einem Anstieg des elektrischen Widerstandes führte. Die Erkenntnisse, die in dieser Diplomarbeit gefunden wurden, können als wertvolle Grundlage für die Weiterentwicklung zukünftiger TiAlNC Schichten dienen.

Table of Contents

1 Introduction 3

2 Theoretical Aspects 5

2.1 Coating Deposition 5

2.2 Physical Vapour Deposition 6

2.2.1 General 6

2.2.2 Plasma 9

2.2.3 Magnetron Sputtering 10

2.3 Coating Formation 11

2.3.1 Nucleation and Growth 11

2.3.2 Structure Zone Models 13

2.4 TiAlN-Coatings 18

2.4.1 General 18

2.4.2 Microstructure 18

2.4.3 Mechanical Properties 21

2.4.4 Influence of Carbon 22

3 Experimental Methods 23

3.1 Coating Deposition 23

3.1.1 Sputtering Equipment 23

3.1.2 Substrates and Targets 24

3.1.3 Coating Deposition Parameters 25

3.1.4 Deposition Procedure 25

3.2 Coating Characterization 26

3.2.1 Ball Crater Technique 26

3.2.2 Scanning Electron Microscopy 27

3.2.3 X-Ray Diffraction 27

3.2.4 Raman Spectroscopy 28

3.2.5 X-Ray Photoelectron Spectroscopy 28

3.2.6 Wafer Curvature Measurements 29

3.2.7 Nanoindentation 31

3.2.8 Four-Point Probe Measurements 31

4 Results 33

4.1 Coating Thickness and Deposition Rate Evaluation 33

4.2 Energy-Dispersive X-Ray Spectroscopy 34

4.3 X-Ray Diffraction....35
4.4 Raman Spectroscopy....38
4.5 X-Ray Photoelectron Spectroscopy....42
4.6 Wafer Curvature Measurements....44
4.7 Nanoindentation....45
4.8 Four-Point Probe Measurements....46

5 Discussion....48

6 Conclusion....51

7 References....52

1 Introduction

The field of coating technology covers a wide range of different processing methods. The common purpose of these methods is to improve the properties of the material surface to resist different loads of mechanical, chemical and thermal nature. Especially hard coatings are becoming increasingly important for tribological applications due to their outstanding properties such as high hardness, excellent wear resistance and chemical inertness. A typical application for hard coatings is wear protection of tools for cutting and forming devices.

A frequently used wear-resistant hard coating is the binary TiN prepared by physical vapour deposition (PVD) or chemical vapour deposition (CVD). Alloying of Al to this binary nitride results in the metastable TiAlN solution, which has a higher wear and oxidation resistance at elevated temperatures. A high potential for further improving the mechanical and thermal properties of TiAlN coatings has been found by alloying elements like Ta, Si, Y, Nb, B, Zr and C to TiAlN. For instance, the addition of C to TiAlN coatings improves properties such as wear and erosion resistance under severe cutting conditions. Due to their outstanding properties, TiAlN based coatings are the focus of numerous scientific studies, for example to further improve their lifetime and performance [1–3].

In this thesis, TiAl alloy targets composed of 50 at.% Ti and 50 at.% Al as well as pure C targets have been used to deposit TiAlNC coatings on Si and MgO substrates by magnetron co-sputtering. By continuously increasing the C target current, coatings with various C contents have been synthesized at 25 and 500 °C, respectively. The major subject of this work was to study the influence of the C content and deposition temperature on the structure development and the mechanical and electrical properties of TiAlN coatings. Several state of the art characterization methods, such as scanning electron microscopy, X-ray diffraction, Raman spectroscopy, residual stress measurements, nanoindentation and electrical resistivity measurements were applied. Subsequenty, limits of C incoperation into the TiAlN phase

could be determined and provide the basis for further improvement of such coating materials.

2 Theoretical Aspects

2.1 Coating Deposition

Generally, vapour deposited coatings have a thickness on the order of several microns or less and may be as thin as a few atomic layers. Such coatings can have completely different properties compared to bulk materials, due to their different microstructure. Figure 1 shows the most important techniques for coating deposition. In principle, deposition processes can be divided into chemical and physical methods. PVD is a frequently applied method for the deposition of hard coatings. A typical example of a PVD technique is magnetron sputtering, which will be the focus of this work; thus its main principles are summarized in the following sections [4,5].

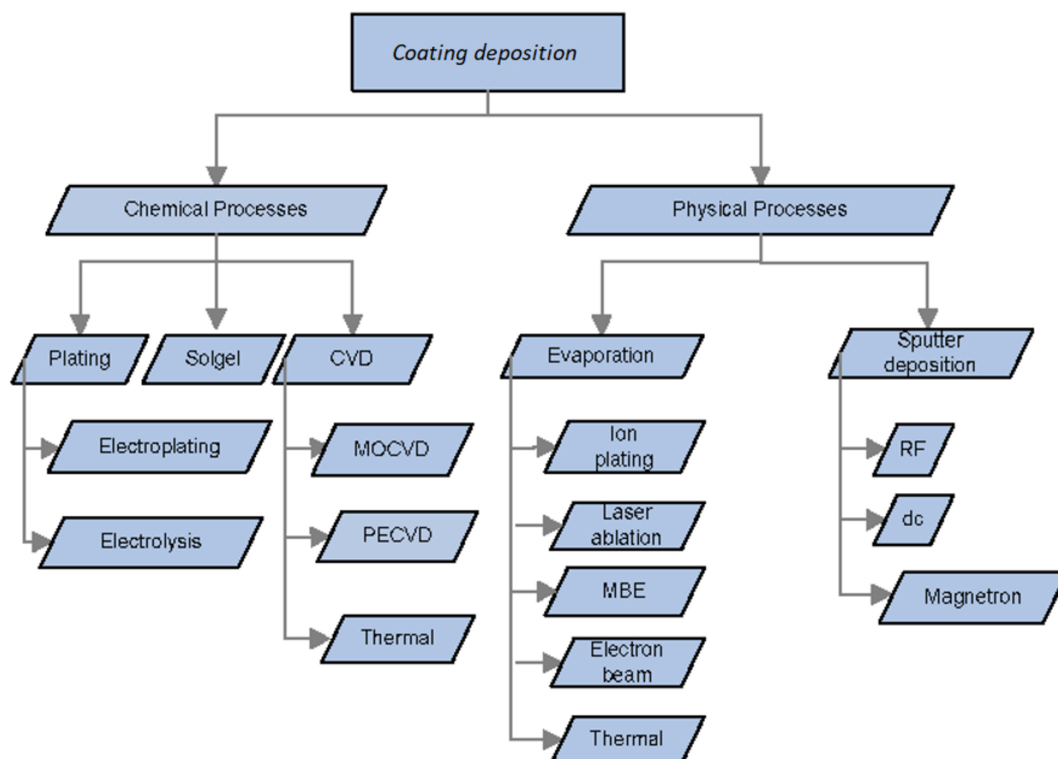

Figure 1 The most important deposition techniques, classified in chemical (left) and physical (right) processes; redrawn after [6].

2.2 Physical Vapour Deposition

2.2.1 General

PVD is used to create coatings by depositing material on almost every technically relevant substrate. For example, metals, ceramics, as well as glass are used as substrates. Since it is possible to deposit coatings either at room temperature or elevated temperatures (up to more than 500 °C), even temperature sensitive substrates, like e.g. plastics, can be used. The process can be applied for the deposition of single and multilayer coatings, for wear resistant coatings, thermal barrier coatings and optical films, etc. The coating process takes place under a low pressure or vacuum environment to prevent uncontrolled air contamination of the coating and to meet the basic requirements for plasma creation. There are three main steps, that describe every PVD process [4,5,7]:

1. Formation of vapour phase.
2. Transport from source to substrate.
3. Film growth on the substrate.

Depending on the method used for converting the solid material into the vapour phase, a classification of the PVD processes can be made into evaporation and sputtering (see Figure 2). Both processes can also be used for reactive deposition. In this case a reactive gas (e.g. Ar) is injected into the vacuum chamber and can form a chemical compound with the elemental target material. Coatings produced by these methods are usually far away from thermodynamic equilibrium. For this reason, they are often characterized by high defect densities and high residual stress, small grain sizes, and/or metastable phases [8,9].

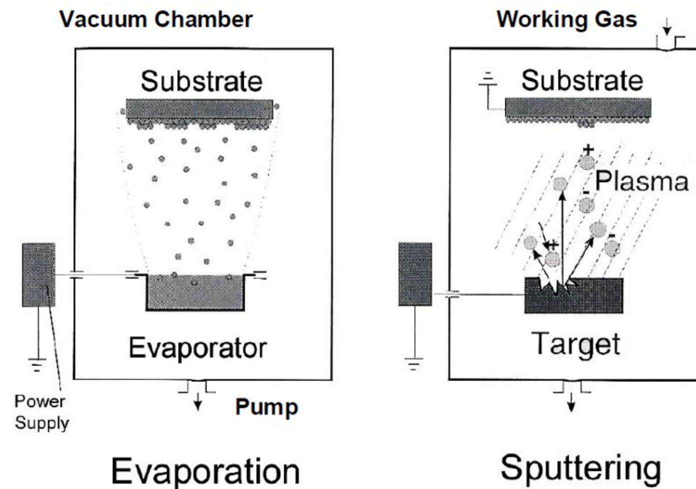

Figure 2 The basic variants of PVD, evaporation and sputtering; redrawn after [5].

Evaporation

During thermal evaporation, the solid or liquid target material is heated until it is transferred to the vapour state, as can be seen in Figure 2. Heating can be performed by resistive or inductive heating, by electron or laser beam heating, or by formation of an arc. Usually, evaporation is carried out under vacuum condition to maximize the mean free path length of vapour particles for negligible particle interactions. The particles transferred into the vapour state move on a straight trajectory towards the substrate and the walls of the vacuum chamber and subsequently form a coating [9].

Sputtering

Sputtering is a physical process which involves the vapourisation of atoms from a surface by momentum transfer from energetic ions bombarding the surface. Coatings of compound materials are produced either by sputtering a compound target or by using an elemental target in reactive gas atmosphere (i.e., reactive sputter deposition) [4].

This technique requires a working gas such as Ar and a high voltage source to generate an electrical field between the substrate and the target or the chamber wall. In direct current (DC)-sputtering, the target can be used as

cathode and the substrate as anode. High energetic Ar^+ ions, generated by collisions of free electrons with neutral particles are accelerated by the electrical field to move towards the negative cathode and bombard the target surface. Surface atoms are ejected when the kinetic energy of the scattered atoms of the collision cascades is higher than their surface binding energy. These knocked-out particles travel from the target towards the substrate, where they can condense as adatoms to form a coating. The number of sputtered atoms ejected per incident ion is defined as the sputtering yield, which mainly depends on the incident ion to target atom mass ratio. Figure 3 shows the general processes that can occur during sputtering [10].

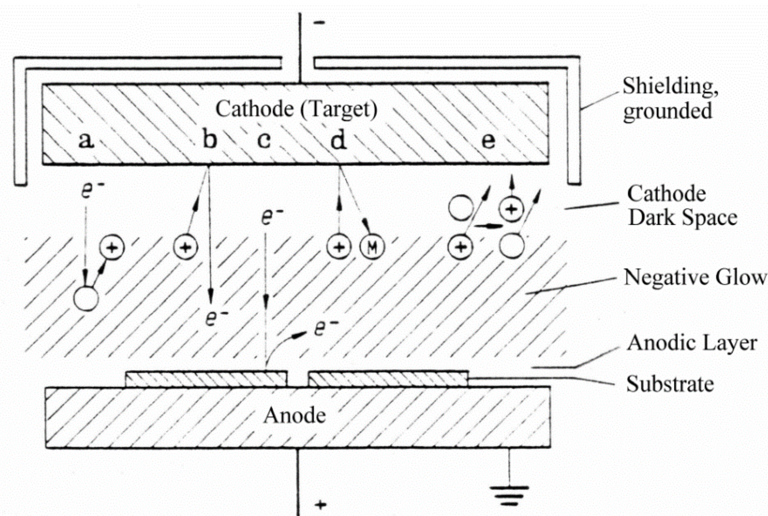

Figure 3 Possible particle interactions during sputtering: Ionisation by electron impact (a), ion induced electron emission from cathode (b), electron induced emission of secondary electrons from anode (c), sputtering caused by ion impact (d), charge transition process (e) [8].

A special form of sputtering is a technique in which a negative voltage is applied between the target and the substrate, which is referred to as bias-sputtering. Due to this bias voltage, charged particles are accelerated towards the growing coating. This can lead to smoother coatings with high residual stress, high hardness and high density due to increased adatom mobility and surface diffusion processes [11].

2.2.2 Plasma

PVD processes usually require a plasma environment. Plasma is an ionized gas, which consists of permanently interacting neutrals, radicals, ions and free electrons. The free electric charges make the plasma electrically conductive and internally interactive, and strongly responsive to an applied electromagnetic field. However, a plasma is in a quasi-neutral state because it consists of equal numbers of positive ions and negative electrons in a sea of non-ionized neutral atoms and molecules (Figure 4a). A simple discharge is shown schematically in Figure 4b. It consists of a voltage source and a low-pressure gas between two parallel conducting plates or electrodes. Plasmas are classified in two different types: non-thermal and thermal plasmas. To produce a non-thermal plasma, which is used in PVD processes, the gas is generally exposed to an electrical or an electromagnetic field. If the voltage is high enough, the gas forms a plasma. Because of inelastic collisions of electrons with neutral gas molecules, more charge carriers are produced. The plasma density is constantly reduced because of energy loss mechanisms such as recombination, radiation and diffusion from the discharge zone. For this reason, an applied electromagnetic field between the electrodes supplies energy to maintain the nonequilibrium state of the plasma. This kind of plasma is usually called cold plasma and is characterized by low temperatures and low pressures [12,13].

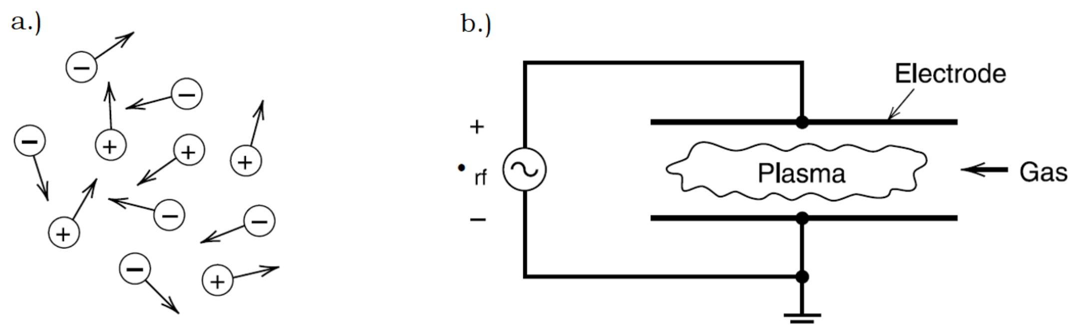

Figure 4 Schematic view of a plasma (a) and a discharge (b) [12].

2.2.3 Magnetron Sputtering

In addition to the applied electric field, a magnetic field is used in the magnetron sputtering process. Strong permanent magnets, so called magnetrons, are located behind the cathode plates. Due to the superposition of the magnetic and electrical fields, the charge carriers (i.e. electrons) are trapped above the target surface. In this way, the local ionisation rate is increased and leads to a higher localised ion density. In turn, this also leads to a significantly enhanced sputtering rate, which results in uneven erosion of the target surface and the formation of so-called racetracks. Magnetron systems are classified into balanced and unbalanced configurations. In a conventional balanced magnetron, all magnetic field lines loop between two magnets and the plasma is trapped at the target area (see Figure 5a). If the magnetic field lines are partially open towards the substrates, as shown in Figure 5b, the configuration is called unbalanced magnetron sputtering. In this case the plasma can expand away from the target area. This effect is achieved by using inner and outer magnets of different strength or by additional electromagnetic coils. Using this configuration enables low-energy ion bombardment of the growing film, thus promoting film growth [8,9].

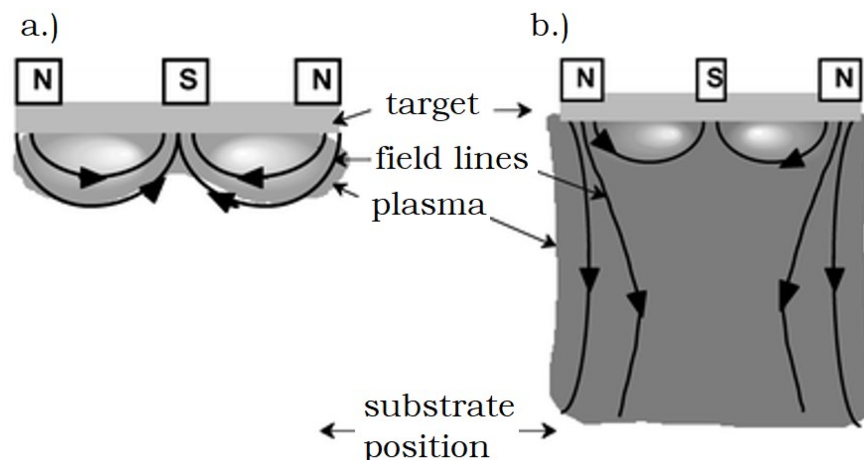

Figure 5 Balanced (a) and unbalanced magnetron sputtering (b) [14].

2.3 Coating Formation

In all application fields of coated materials, it is required to have a sufficiently high coating adhesion to the substrate. The coating adhesion depends mainly on the selected material partners, the deposition parameters as well as on the pre-treatment of the substrate [8].

2.3.1 Nucleation and Growth

After converting the target material into the vapour phase, these atoms may collide with the substrate surface or the surface of the deposition chamber. If the ejected atoms reach the substrate, two different processes are possible. They can be either reflected directly or they condense as loosely bound adatoms. As adatoms, they diffuse along the surface until they either re-evaporate or become trapped at low-energy lattice sites, such as surface discontinuities. Several adatoms can agglomerate and form stable clusters, the so-called nuclei, which is then referred to as nucleation. Further film growth occurs through adsorption of further adatoms from the surface or directly from the gas phase. During coating deposition interdiffusion occurs, thus substrate and film atoms exchange sites and the film/substrate interface is smoothened (Figure 6) [10].

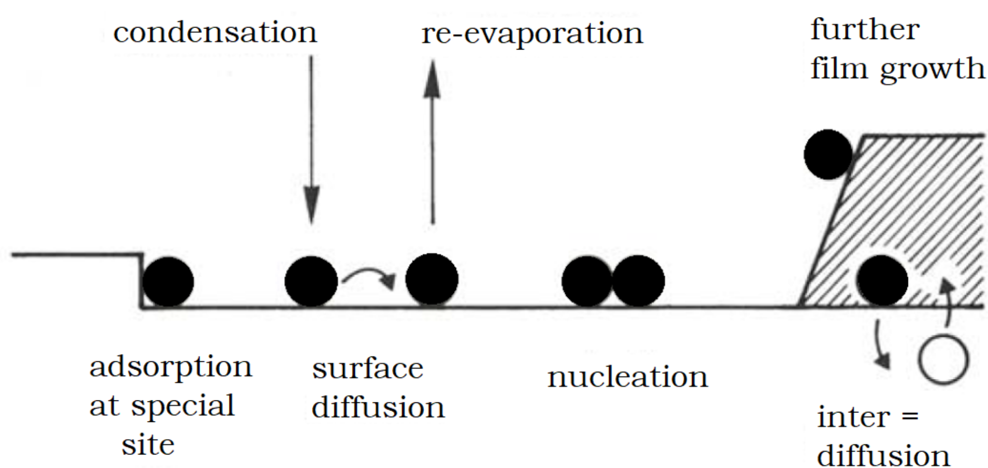

Figure 6 Schematic representation of atomic processes involved in thin film growth. Substrate atoms shown as white and film atoms as dark circles [15].

The surface mobility of the adatoms is determined by their kinetic energy, the substrate temperature and the attraction forces between adatom and substrate. Strong attraction forces between the adatom and the substrate lead to a high nucleus density (number of nuclei per unit area) on the surface. Vice versa a week interaction leads to a low nucleus density on the surface. Depending on the condition, the nuclei coalesce into a more or less continuous layer[8].

In Figure 7 the three basic growth modes are shown: Island growth (Volmer-Weber), layer growth (Frank-Van der Merwe) and mixed layer-island growth (Stranski-Krastanov). The attraction forces between neighbouring film atoms exceed the forces between film atoms and the substrate in the island growth mode. In the opposite case, the attraction forces between layer and substrate atoms are stronger than between neighbouring layer atoms, which leads to layer by layer growth. Each new layer only starts to grow if the last one has been finished. The layer-island growth is an intermediate case, where one, or sometimes several complete monolayers are formed; but then further layer growth becomes unfavourable and island growth occurs [10,15].

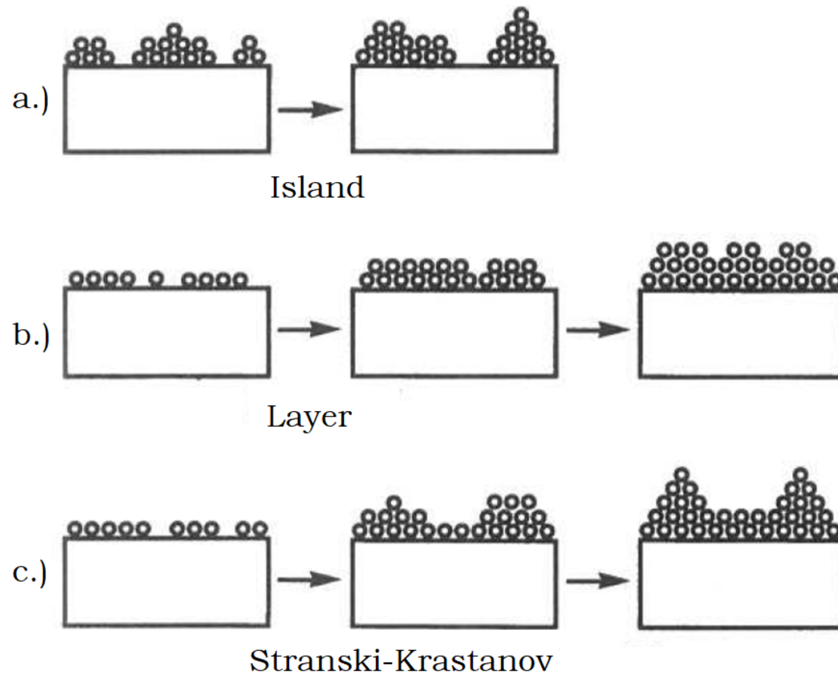

Figure 7 The three basic modes of thin film growth mechanisms: Volmer-Weber (island growth) (a), Frank-Van der Merwe (layer-by-layer growth) (b) and Stranski-Krastanov (layer-island growth) (c) [10].

2.3.2 Structure Zone Models

A suitable way to illustrate the correlation of the microstructure of vacuum-deposited layers and deposition parameters are so called structure zone models (SZM). These models demonstrate the structure change with respect to deposition parameters, such as gas pressure or bias voltage [16].

The layer growth and the layer structure also depend on the roughness of the substrate surface, activation energies for surface and bulk diffusion of the layer atoms and the interactions between layer and substrate atoms. Due to the roughness of the substrate surface, generally a non-uniform growth of the coating is observed. The resulting shading effect leads to formation of porous structures, which can be compensated by surface diffusion processes of the adatoms. The substrate temperature T_S or the substrate temperature relative to the melting point T_S/T_m (i.e. homologous temperature) can be used as a measure for the activation energies of the diffusion processes [8].

The first SZM was proposed by Movchan and Demchishin in 1969 based on observations of very thick evaporated metal and oxide coatings. Depending on the homologous temperature, three characteristic microstructures are found within the SZM (Figure 8). Each zone has its own characteristic structure with corresponding properties. In the first zone ($T_S/T_m<0.3$) the structures are columnar, consisting of inverted cone like units capped by domes and separated by voided boundaries, that are several nanometers wide. Because of the low temperature this structure arises from shadowing effects and very limited adatom motion. A further effect of the low temperatures is the limited surface diffusion and that almost no bulk diffusion is taking place. The second zone can be observed at higher temperatures ($0.3<T_S/T_m<0.45$) and is favoured by surface and grain boundary diffusion. The coating's structure is still columnar but with more dense grain boundaries. Zone three finally covers the temperature range in which bulk diffusion is possible ($T_S/T_m>0.5$). This leads to a recrystallized dense structure whih exhibits rather large, equiaxed grains [10,17].

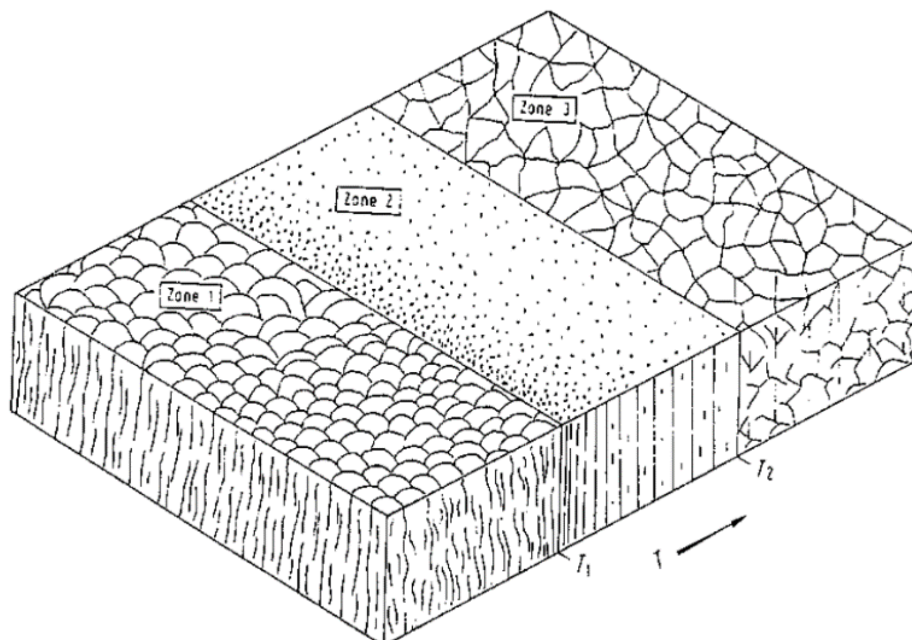

Figure 8 Influence of deposition temperature on the microstructure of the evaporated coatings according to the SZM of Movchan and Demchishin [8].

The Movchan and Demchishin SZM was later extended by Thornton. In order to take the effect of the sputter gas pressure in account, Thornton expanded the structure zone diagram by an additional axis. Figure 9 illustrates the four different areas of the Thornton SZM. Thornton added also an additional transition zone (zone T) between zone one and zone two. In zone one the mobility of the adatoms is not sufficient to compensate shading effects because of the low temperature. The structure consists of conical crystallites and is characterized by pores at the grain boundaries. Due to surface diffusion, the shading effects are partially compensated in zone T. A cone shaped columnar structure is typical for coating deposition within this zone. In zone two the surface diffusion is decisive for the growth mechanism. A columnar structure is formed whereby the column diameter grows with increasing the substrate temperature and the porosity decreases correspondingly. In zone three, lattice and grain-boundary diffusion processes dominate because of the high substrate temperatures. This leads to a recrystallized, coarse-grained, dense structure of the coating [8,18].

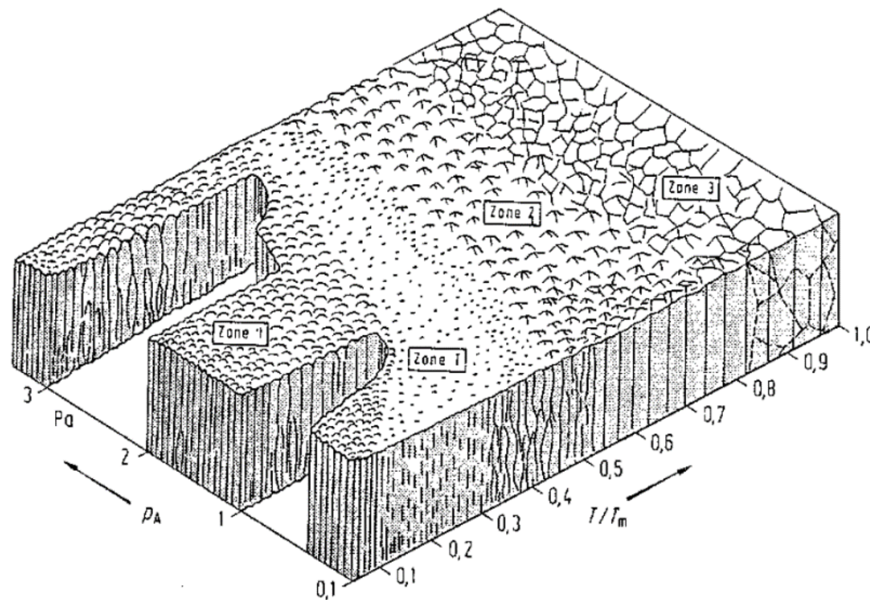

Figure 9 Extended SZM according to Thornton for sputtered coatings showing four zones with different coating morphologies as a function of the homologous temperature and the gas pressure [8].

Later Messier et al. [19] proposed a SZM for ion plating that characterizes the coating microstructure as a function of temperature and bias potential as shown in Figure 10. By increasing the bias potential, ions are accelerated from the plasma to the substrate, resulting in a high nucleation density. With increasing energy of the accelerated ions, the zone boundary between zone one and zone T shifts to lower temperatures.

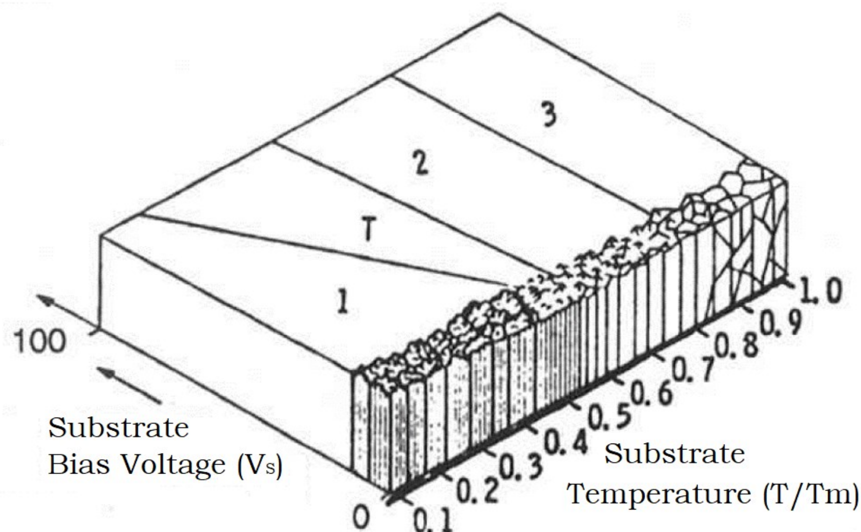

Figure 10 SZM according to Messier et al. showing the coating morphology as a function of the homologous temperature and the bias voltage [10].

The structure evolution of coatings is also influenced by impurities. In the previous structure zone models this parameter was not considered, thus other “real” SZM´s have been developed. SZM´s with different impurity concentrations are shown in Figure 11. At low impurity levels (Figure 11b) and very low temperatures (zone one), the process induced segregation of impurities can be negligible and the impurity species can be incorporated into the growing lattice of fibres. Compared to the ideal structure model (Figure 11a), the density of nucleation can be primarily influenced by the impurities [20].

Figure 11 b-d illustrates zone one shifting to higher and zone three to lower temperatures with a higher degree of impurities. Due to these impurities, the diffusion is limited and therefore zone two and zone three are shifted to

higher temperatures until they finally completely disappear at a very high impurity concentration. At a high impurity level, equiaxed grains with different grain sizes can be observed. Because the volume of the impurity phase becomes comparable to the volume of the deposited material at a very high impurity content, microcrystalline, nanocrystalline and finally amorphous structures develop [20].

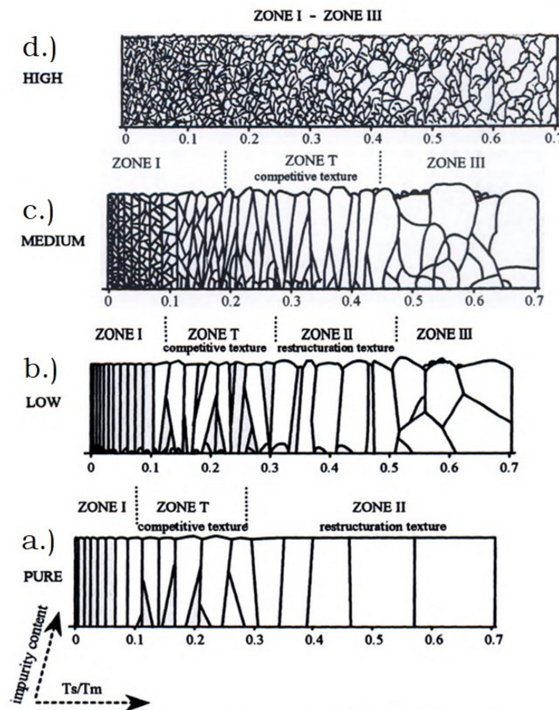

Figure 11 Ideal and real SZM´s as a function of the homologous temperature and pure (a), low (b), medium (c) and high (d) impurity content [16].

2.4 TiAlN Coatings

2.4.1 General

In the 1980´s, titanium nitride (TiN) was the most commonly used hard coating for cutting applications. The substance offered favourable properties such as high hardness and excellent wear resistance. However, TiN coatings have a limited live time at higher temperatures. In ambient air, at temperatures above 500 °C, oxidation takes place and a brittle and porous TiO_2 phase (rutile) is formed, which deteriorates the mechanical properties and limits the lifetime of the cutting tools. By incorporating aluminium into the TiN lattice, the oxidation resistance can be shifted to temperatures of 700 °C or higher. This is possible due to the formation of an dense Al_2O_3 protective layer on the coating surface at elevated temperatures. Thus, avoiding further oxygen diffusion into the coating effectively prevents oxidation. Moreover, the coating system provides higher hardness, a lower friction coefficient at elevated temperatures and a lower thermal conductivity [21–24].

2.4.2 Microstructure

In thermodynamic equilibrium, the metastable Ti-Al-N system can be assessed by the ternary phase diagram. An isothermal section of the ternary phase diagram at 1000 °C is illustrated in Figure 12. This diagram reveals the very low solubility of Ti in AlN, Al in TiN and N in TiAl. However, at thermodynamic equilibrium two ternary stable phases with the atomic order exist: Ti_3AlN and Ti_2AlN. Ti_3AlN has a cubic perowskite-type structure with a lattice parameter of 4.11 Å, while Ti_2AlN has a hexagonal structure with lattice constants a = 2.99 Å and c = 13.62 Å [1,25].

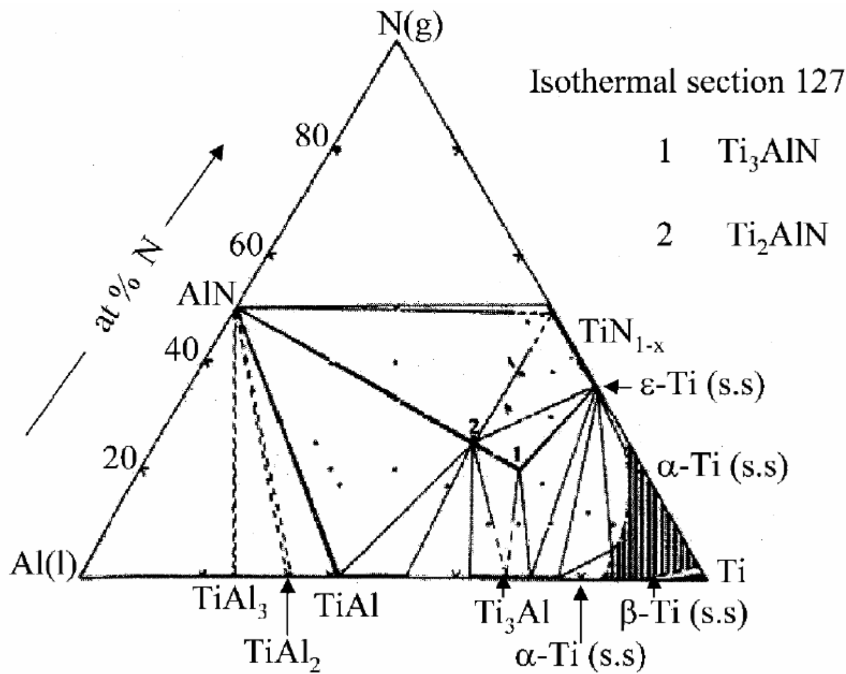

Figure 12 Isothermal section of the ternary phase diagram Ti-Al-N at 1000°C [25].

In Figure 13 the quasi-binary system TiN-AlN derived from the ternary Ti-Al-N system is illustrated. This diagram visualises an eutectic dual phase system, in which the cubic (c)-TiN and the hexagonal (hex), also called wurtzite (w)-AlN are in equilibrium as a dual phase mixture. Both phases, c-TiN and w-AlN, are separated over the whole temperature range showing a poor solubility of each phase in another. The maximum solubility of w-AlN in c-TiN is only about 5 mol.% at 2750 °C [1,26].

Figure 13 Quasi-binary phase diagram TiN-AlN revealing a dual phase mixture of c-TiN and w-AlN with only minor solubility of one into each other [26].

As previously mentioned, growth of PVD coatings is thermodynamically a non-equilibrium process. Because of the high energy bombardment and the relatively low deposition temperatures it is possible to create supersaturated metastable solid solutions. Al atoms can incorporate into the c-TiN lattice according to Figure 14. At low Al contents, the Ti atoms are substituted by Al atoms and a c-TiAlN lattice is formed. However, further increasing the AlN fraction yields a dual phase structure followed by single phase w-TiAlN, where substitution of Al by Ti atoms in the w-AlN lattice occurs. The Al fraction where the crystal structure of c-TiAlN changes into the two phased c-TiN and w-AlN structure ranges from approximately 0.65 to 0.75 [1,27].

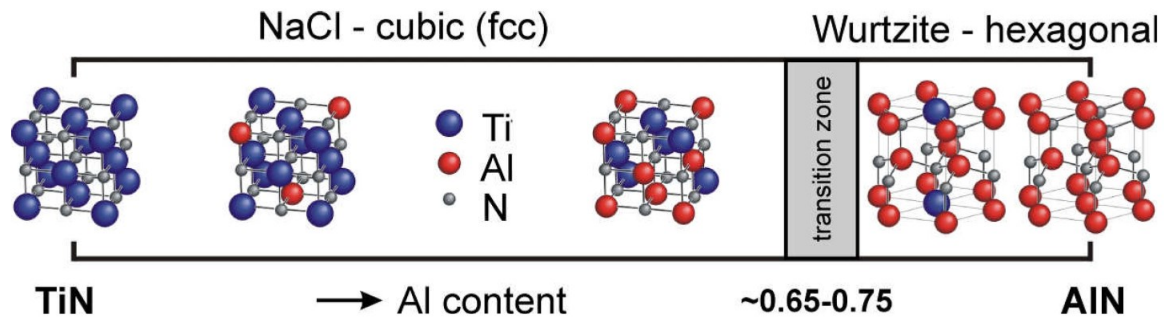

Figure 14 Structural development from c-TiN to w-AlN [27].

2.4.3 Mechanical Properties

TiAlN coatings are characterized by their high hardness, good oxidation resistance, thermal stability, good wear resistance and low thermal conductivity. The hardness and the Young´s modulus strongly correlate with the Al content in the coating (see Figure 15). With increasing Al content, the hardness and the Young´s modulus rise until a maximum at approximately 50 mol.% is reached. The high hardness results from the solid solution strengthening due to incorporation of Al atoms in the TiN lattice. Further increasing the Al content leads to a significant decrease of the Young´s modulus and the hardness because of formation of the softer w-AlN phase [1,28,29].

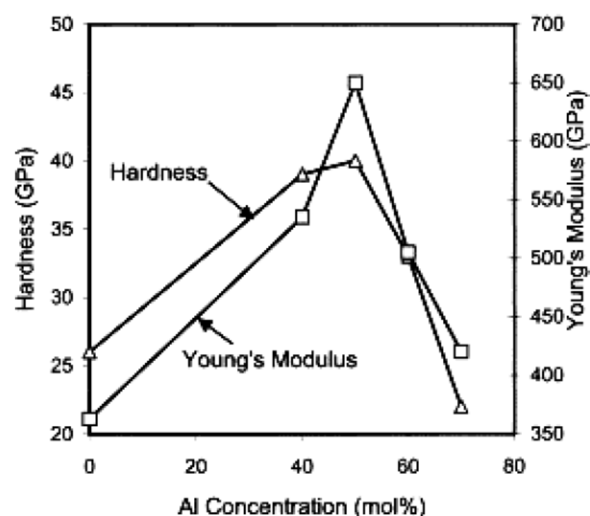

Figure 15 Hardness and Young´s modulus as a function of the Al concentration in TiAlN coatings [29].

Another mechanism that can increase the mechanical properties of coatings is age hardening. The metastable c-TiAlN system decomposes spinodally into c-TiN (rich) and c-AlN (rich) domains at temperatures between 600 °C and 1000 °C. Due to coherent precipitation of the c-AlN phase, this also results in an pronounced increase of the hardness. At a further temperature increase, these metastable c-AlN domains transform into the stable w-AlN, resulting in a significant decrease in hardness. Carefully adjusting the deposition paramters might allow to shift the Al conentration of the single phase c-TiAlN to higher values and retard the onset of spinodal decomposition and subsequent transformation at elevated temperatures [27,30].

2.4.4 Influence of Carbon

C is a chemical element and has a ground state electron configuration of $1s^2 2s^2 2p^2$. With its four outer valence electrons it is able to from three different hybrid bonds, i.e. sp^3, sp^2 and sp^1 bonds. One of the crystalline forms of C is diamond, where all bonds exhibit the sp^3 configuration. Due to this strong bonding type, diamond has a high bulk modulus, density and thermal conductivity. In contrast to diamond, graphite has an sp^2 configuration, is a good electrical conductor and has outstanding properties as a solid lubricant. The bonding type of amorphous carbon (a-C) is a mixture of sp^2 and sp^3 bonds. Depending on the sp^2/sp^3 ratio, the properties of a-C might resemble either those of diamond or graphite. If C is added to the TiAlN system, only a small amount of C atoms can be dissolved as interstitials. With further increasing the C content, the solubility limit within the TiAlN lattice is reached and precipitation of a C phase occurs. If C precipates as a-C, the transition between crystalline and amorphous microstructure can be used to provide coatings with various properties such as higher hardness, higher thermal and electrical conductivity and wear resistance [3,31,32].

3 Experimental Methods

3.1 Coating Deposition

3.1.1 Sputtering Equipment

The investigated coatings of this work were deposited in a laboratory scale unbalanced DC magnetron sputtering system. Argon was chosen as working and nitrogen as reactive gas. As shown in Figure 16, the cylindrical vacuum chamber (Ø 380 mm x 235 mm) consisted of a sample holder, an AJA magnetron cluster (3 magnetrons equipped with 2 targets), the power supply for the magnetrons and the gas inlet systems.

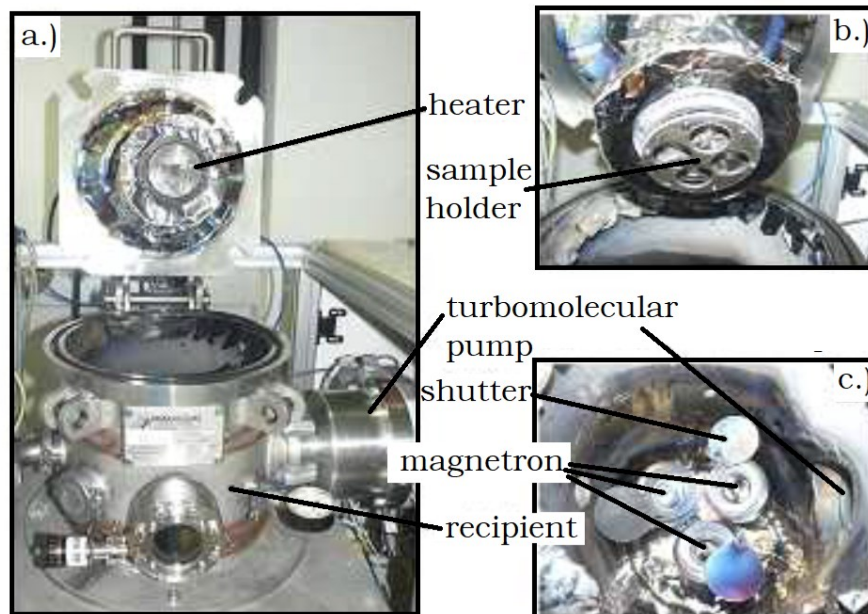

Figure 16 Laboratory scale high-vacuum unbalanced DC magnetron sputtering system (a), rotating sample holder (b) and three magnetrons with moveable shutters (c).

The magnetron power sources for the targets were two bipolar pulsed DC power generators (ENI RPG-50, programmable frequency 50-250 kHz, duty cycle from 2.5 to 40%), which can operate in DC and pulsed DC mode. A third pulsed DC generator (ENI RPG-50) was used to apply a negative voltage to the substrate for the plasma etching process prior to deposition and to

apply a negative bias voltage during deposition. The evacuation system consisted of a dual stage rotary vane pump (Pfeiffer Vacuum Duo 20, pumping speed 24 m^3/h N_2) and turbomolecular pump (Pfeiffer Vacuum TMH 521 P, pumping speed 1080 m^3/h N_2). The lower part of the chamber consisted of 3 water-cooled targets (Ø 50.4 mm), which can be closed by shutters (Figure 16c). The upper part contained the substrate holder, which can be heated up to 700°C during rotation (Figure 16b).

3.1.2 Substrates and Targets

Table 1 displays the used substrates, their dimensions and purpose of their usage.

Table 1 Substrates used within this thesis.

Substrates	**Orientation**	**Dimensions [mm]**	**Intended purpose of investigation**
Si	100	20 × 7.2 × 0.32	Thickness evaluation, SEM, XRD, Raman, XPS, BSM, nanoindentation
MgO	100/110/111	10 × 10 × 0.5	XRD, electrical resistivity

Two different types of targets were necessary for the coating process: Ti(50)/Al(50) at.% and C(100) at.% targets (Ø 50.4 mm × 6.35 mm) with a purity of 99.9 and 99.99 %, respectively. Both targets were produced by the FHR centrotherm group, Germany.

3.1.3 Coating Deposition Parameters

As previously mentioned, Ar with a purity of 99.9 % and N_2 with a purity of 99.5 % were used as process gases in all coating series. The reactive gas flow rate (N_2) and the work gas flow rate (Ar) were set to 10 sccm and 30 sccm, respectively, to guarantee a constant chamber pressure of approximately 1 Pa. A current $I_{Ti/Al}$ of 0.25 A was kept constant on the Ti/Al target. The C magnetron current I_c was increased in 0.02 A steps from 0 to 0.2 A. During the deposition time of 120 min, a bias voltage of -100 V was applied. Two coating series with 11 specimens each were deposited at 25 and 500 °C, respectively.

3.1.4 Deposition Procedure

The deposition of the TiAlNC coatings was performed by the following steps:

- Prior to the coating process, the substrates were cleaned ultrasonically in acetone for 10 min.
- After drying, the substrates were fixed to the sample holder and mounted within the deposition chamber.
- When the pressure reached 2×10^{-3} Pa, the chamber was heated to 500 °C. In contrast, the chamber was not heated for the 25 °C series.
- After the temperature of 500 °C in case of the high-temperature series or 25 °C for the room-temperature series and a pressure of 2×10^{-3} Pa were reached, the substrates were plasma etched: There, a plasma was ignited in pure argon atmosphere. The etching voltage and the etching frequency were set to -500 V and 250 kHz, respectively. The etching time was 1 min. During the etching process, the rotation of the sample holder was turned on.
- Subsequently, the deposition parameters were adjusted. The shutters of the C and the Ti/Al target were removed and the deposition process was started. Additionally, the substrates were biased with a bias voltage of -100 V. N_2 and Ar flow rate were set to 10 sccm and 30 sccm during the deposition process.

- When the deposition process was finished, the power supplies, the sample holder rotation and the heating system were turned off. After cooling down to 50 °C the pumping system was shut off, the chamber was vented and the substrates were dismounted.

3.2 Coating Characterization

3.2.1 Ball Crater Technique

The coating thickness is a necessary information for all further investigations. It is required for the evaluation of experimental data obtained from residual stress measurements, nanoindentation and electrical resistivity. Furthermore, the coating thickness gives information about the growth kinetics, i.e. the deposition rate. A common method to determine the coating thickness is the ball crater technique (Calo®-test). This test uses a rotating steel ball and a diamond suspension to grind a wear crater with the shape of a spherical calotte through the coating into the substrate. A schematic view of this test is shown in Figure 17. Subsequently, the coating thickness is calculated with the following reduced equation [33,34]:

Equation 3-1

$$t_c = \frac{Do^2 - Di^2}{4D}$$

with the outer and inner diameter of the calotte Do and Di , respectively, the ball's diameter D and the coating thickness t_c. Within this thesis, a steel ball with a diameter D of 25.4 mm and diamond suspension with a particle size of 3 µm were chosen.

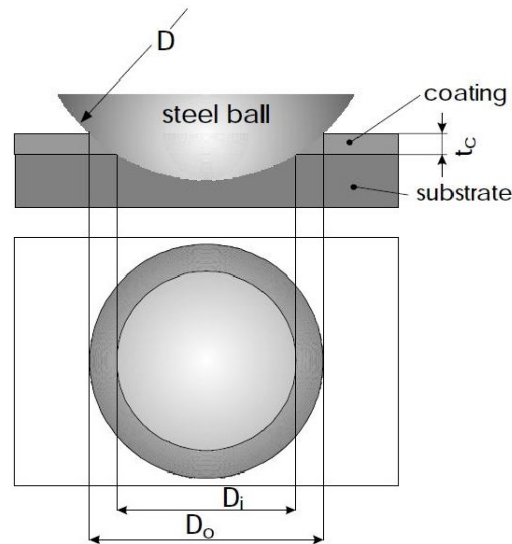

Figure 17 Schematic view of the ball-crater-test and the generated calotte [33].

3.2.2 Scanning Electron Microscopy

To determinate the chemical composition of the coatings, energy-dispersive X-ray spectroscopy (EDS) utilizing an Oxford Instrument INCA system in a Zeiss EVO 50 scanning electron microscope (SEM) was used. The acceleration voltage was set to 10 kV and the implemented standards of the SEM were applied.

3.2.3 X-Ray Diffraction

To determine the crystallographic structure of all coatings, X-ray diffraction (XRD) was carried out with a Bruker-AXS D8 Advance diffractometer using Cu Kα radiation (λ = 0.154 nm). The diffractograms were recorded in θ/2θ geometry with a 2θ angle between 20 and 85°. The operating parameters are summarized in Table 2.

Table 2 Operating parameters of the Bruker-AXS D8 Advance diffractometer.

High Voltage [kV]	**Tube Current [mA]**	**Step Time [s]**	**Step Size 2θ [°]**
40	40	1.2	0.02

3.2.4 Raman Spectroscopy

The Raman effect is based on the interaction between light and matter. Light which is generated by a laser stimulates molecules of the sample. By analysing the scattered light, which has a different wavelength than the excitation spectrum (i.e. inelastic scattering of sample molecules), information on the chemical and physical properties of crystalline as well as amorphous samples can be obtained. Raman spectroscopy allows the identification of very low-concentration phases as well as structural characterization and qualitative determination of the crystallinity, orientation and composition of materials. In this work Raman spectroscopy was used to determine the ratio of I_D/I_G , which means to estimate the ratio of sp^3/sp^2 content of the coatings. Raman spectra were acquired with a Jobin Yvon Labram confocal spectrometer, which was equipped with a frequency-doubled ND-YAG laser (100 mW, 532.2 nm, Ø6 µm) and a CCD matrix-detector over 1 mm × 1 mm. The intensity of the laser was reduced with different filters to avoid damaging the coatings [35].

3.2.5 X-Ray Photoelectron Spectroscopy

X-ray photoelectron spectroscopy (XPS) can be used to determine the chemical and the electronic state of a material. During XPS, the surface of a sample is irradiated with an X-ray beam which causes excited electrons to escape from the sample surface. These electrons are detected and simultaneously their kinetic energy is measured. In this thesis, XPS was used to determine the contribution of the binding energy E_B of the carbon C1s orbital. The measurements were carried out with a Thermo-Scientific K-Alpha X-ray photoelectron spectrometer. The operating parameters are listed in Table 3. XPS depth profile measurements were carried out using an Ar^+ ion sputtering gun operated at 5 keV and 0.5 mA for 3 min.

Table 3 Operating parameters for XPS.

Source Type	**Spot Size [µm]**	**Lens Mode**	**Analyser Mode [eV]**	**Energy Step Size [eV]**
Al Kα	400	Standard	CAE : Pass Energy 50.0 eV	0.1

3.2.6 Wafer Curvature Measurements

The formation of stress states in the coatings has several causes. In general, three effects may contribute to macroscopic residual stress states: The intrinsic, extrinsic and thermal residual stresses. The intrinsic residual stresses are generated during the growth process and depend strongly on the growth conditions. Extrinisic stresses can arise due to the structural misfit, phase transformations or precipation. Stresses induced by different thermal expansion coefficients between the substrate material and the coating are an example for thermal residual stresses [36,37].

The biaxial stress measurements were carried out by measuring the curvature of coated Si substrates at room temperature. Compressive stress leads to a concave curvature (Figure 18a), whereas tensile stress leads to a convex curvature of the sample (Figure 18b). The principle of the measurement is shown in Figure 18c.

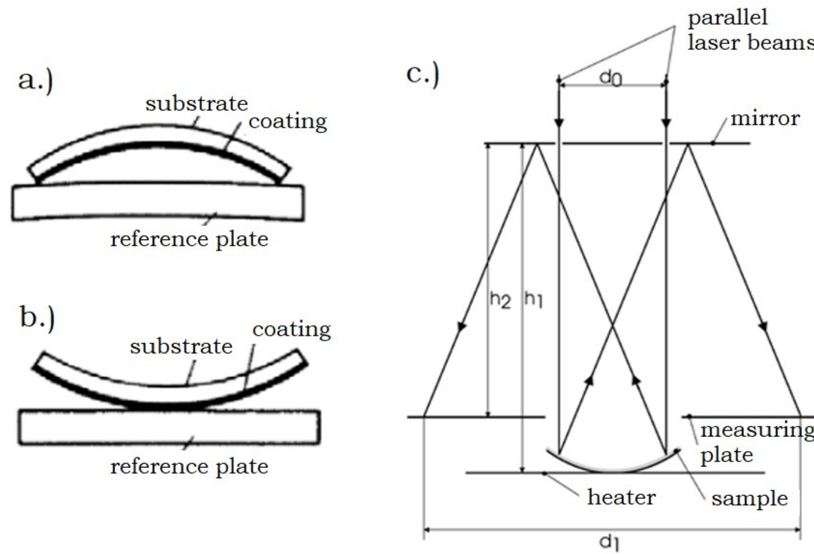

Figure 18 Schematic representation of a coated substrate with tensile stresses (a) and compressive stresses (b) in the layer. Principle of the curvature measurement via two parallel laser beams (c) [36].

Two parallel He-Ne-laser beams are used to measure the radius of curvature. These beams are focussed on the sample surface, subsequently reflected to a mirror and then reflected again onto the measuring plate. The diverted beam distance d_1 can be measured and the radius of curvature r of the coated substrates is given by Equation 3-2.

Equation 3-2

$$r = \frac{2(h_1 + h_2)d_o}{d_o + d_1}$$

There, h_1 and h_2 are the source to sample distances, d_o is the initial distance between the two laser beams and d_1 is the measured distance after reflection. The radius of curvature is used to determine the magnitude of the residual biaxial stress by means of the modified Stoney equation [38].

Equation 3-3

$$\sigma = \frac{1}{6} * \left(\frac{E_s}{1 - v_s}\right) * \frac{{t_s}^2}{t_c} * \frac{1}{r}$$

In this equation E_s represents the biaxial modulus of the (100) orientated silicon substrate, υ_s is the Poisson ratio of the substrate, t_s and t_c are the thickness of the substrate and the coating.

3.2.7 Nanoindentation

Nanoindentation was used to measure the hardness and Young´s modulus of the coatings. The properties were quantified with a UMIS Nanoindenter (Ultra Micro Indentation System) from Fischer-Cripps Laboratories, equipped with a diamond Berkovich indenter. All experiments were evaluated according to Oliver & Pharr [1] using the software package IBIS. The samples were mounted onto a specimen holder and acclimatised in the sample chamber. The indentation depth was controlled by the "rule of thumb" that the maximum depth value must not exceed 10 % of the coating thickness [39]. Within this thesis a plateau test from 15 to 5 mN in steps of 0.5 mN was carried out for each sample. Thus, 20 individual indents were recorded for each sample and at least 10 were taken into account for the evaluation.

3.2.8 Four-Point Probe Measurements

By using a Jandel four-point probe, the resistivity of all coatings was determined. The principle of a four-point system is based on the measurement of the area resistivity. As shown in Figure 19, the test arrangement consists of four equal tips. A DC current is applied by the outer tips, while the inner tips are used to measure the voltage. The following equation provides the calculation of the electrical resistivity ρ [40]:

Equation 3-4

$$\rho = \frac{\pi t}{ln2} * \frac{V}{I}$$

with the coating thickness t, the voltage V and the current I.

Each coating was measured two times in the centre of the specimen. Only voltage values constant over a relevant period of 5 s were taken for further calculations.

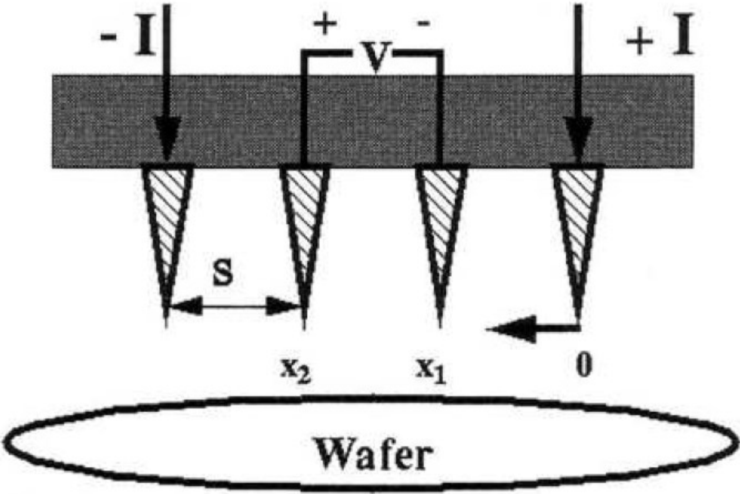

Figure 19 Schematic image of the electrical four-point probe test.

4 Results

4.1 Coating Thickness and Deposition Rate Evaluation

The coating thickness with respect to increasing current on the C target, measured on silicon samples, is displayed in Figure 20a. A general increase with increasing current on the C target can be observed. The coatings deposited at 25 °C show thickness values ranging from 0.58 to 1.95 µm and the 500 °C series varies between 0.61 and 1.71 µm. With the coating thickness and the deposition time, the deposition rate can be calculated, which is displayed in Figure 20b for the coatings deposited at 25 and 500 °C, respectively. Due to the constant deposition time, the deposition rate shows a similar trend as the coating thickness. With increasing current on the C target a significant rise is observed. Coatings deposited at 25 °C exhibit deposition rates ranging from 0.08 to 0.27 nm/sec. At a deposition temperature of 500 °C a minor decrease of the deposition rate, ranging from 0.08 to 0.24 nm/sec is observed.

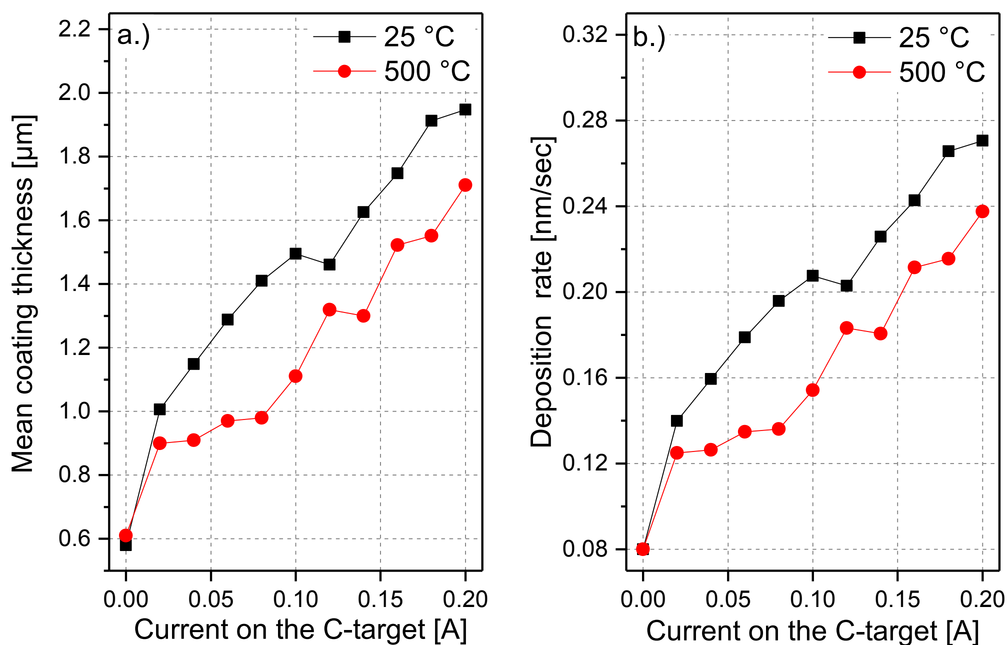

Figure 20 Coating thickness as a function of the current on the C target (a) and deposition rate versus the current on the C target (b).

4.2 Energy-Dispersive X-Ray Spectroscopy

The elemental composition of the coatings was determined via energy-dispersive X-ray spectroscopy (EDS); the obtained results are presented in the following section. Table 4 shows the elemental composition of all coatings with increasing current on the C target. The results show that the main elements of the TiAlNC coatings are C, N, Al, Ti, and a low amount of O. The C content in the deposited coatings increases with increasing current on the C target. It increases in a wide range from 0.00 to 36.1 at.% and from 0.0 to 35.2 at.% within the coatings deposited at 25 and 500 °C, respectively. However, coatings deposited at 500 °C exhibit significantly less C up to a C target current of 0.8 A. The N, Al and Ti content simultaneously decrease with increasing current on the C target, i.e. C content. The O content of the coatings remains constant regardless of alteration of current on the C target.

Table 4 Summary of the EDS results representing the elemental composition of the coatings.

T_{dep} [°C]	**Current C-Target [A]**	**C [at.%]**	**N [at.%]**	**O [at.%]**	**Al [at.%]**	**Ti [at.%]**
25	0.00	0.0	51.2	4.0	24.8	19.9
	0.02	8.5	50.3	4.3	21.5	15.3
	0.04	11.8	49.8	2.5	20.8	15.2
	0.06	15.6	49.5	1.2	19.6	14.0
	0.08	18.9	45.6	4.4	18.1	13.1
	0.10	21.8	41.9	9.2	15.6	11.5
	0.12	24.9	40.0	8.7	15.3	11.1
	0.14	27.6	39.1	8.8	14.3	10.3
	0.16	30.1	40.7	5.7	13.5	10.1
	0.18	33.4	40.6	3.5	13.0	9.6
	0.20	36.1	39.8	2.4	12.2	9.4
500	0.00	0.0	50.1	4.0	25.5	20.3
	0.02	5.0	50.1	4.8	24.2	15.9
	0.04	5.6	47.7	7.3	23.4	16.0
	0.06	8.7	47.1	6.1	22.9	15.2
	0.08	14.9	46.3	1.7	22.0	15.2
	0.10	18.8	44.1	1.1	21.0	14.9

0.12	21.9	44.1	2.1	18.8	13.2
0.14	26.5	42.5	1.9	17.4	11.8
0.16	29.5	41.2	2.2	15.8	11.5
0.18	32.4	40.3	1.4	15.2	10.9
0.20	35.2	38.6	1.2	14.6	10.4

4.3 X-Ray Diffraction

Within this chapter, the results of the X-ray diffraction (XRD) measurements are shown for the 25 °C and the 500 °C series at different C contents. In order to illustrate the influence of the C content, the X-ray diffractograms are arranged one above the other (Figure 21 and Figure 22). The standard peak positions are indicated by droplines: black short dashed lines denote the hex-AlN peaks (ICDD 00-025-1133), red dashed lines the fcc-AlN peaks (ICDD 00-046-1200) and blue dashed dotted lines the fcc-TiN peaks (ICDD 00-038-1420). At the 2θ angle of 70 °, a large diffraction peak can be found, which can be related to the Si substrate. Generally, in all patterns a shift of the coatings derived from the coating can be observed compared to the standard peak positions. As shown in Figure 21, the reference coating without C exhibits only a single diffraction peak at the 2θ angle of approximately 42.6 °. This peak can be related to the fcc-TiAlN phase indicating a (100) preferred orientation. With increasing C content, the fcc-TiAlN (200) peak disappears and a diffraction peak at the 2θ angle of 37.2 ° can be observed. This peak can be related to fcc-TiAlN (111) indicating a change in the preferred orientation. With further increase of the C content, the fcc-TiAlN (111) peak disappears and no diffraction peaks are detected in coatings with a C content above 11.8 at.% C.

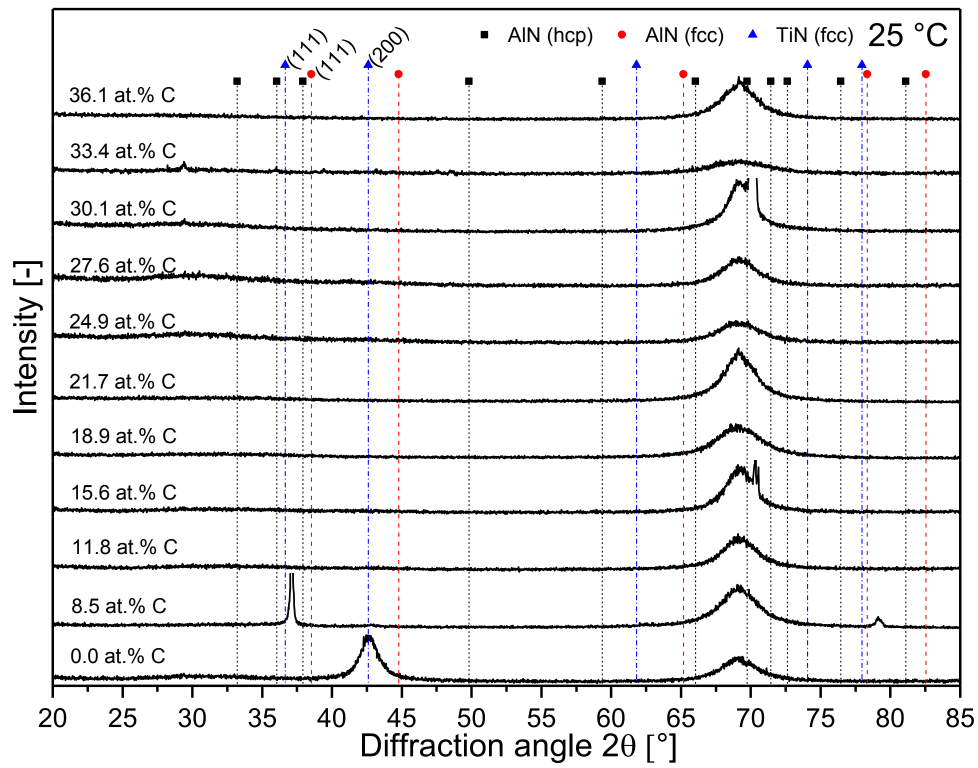

Figure 21 XRD patterns of TiAlNC coatings with various C contents deposited at 25°C on Si (100) substrates.

Figure 22 illustrates the XRD patterns of the coatings deposited at 500 °C. The reference coating without C only exhibits a diffraction peak at the 2θ angle of 43.1 °, which can be again related to the fcc-TiAlN phase indicating a (100) preferred orientation. At a C content from 5.0 to 14.9 at.% diffraction peaks at an 2θ angle of 37.3 ° are observed, which can be related to fcc-TiAlN (111). Details of the diffractogramms of the coatings with a C content ranging from 5.01 to 18.8 at.% are shown in enlarged scale in Figure 23. Increasing the C content up to 18.8 at.% leads to a significant decrease of the fcc-TiAlN peak intensities. Furthermore, a shift of the (111) diffraction peak towards lower diffraction angles is observed with increasing C content. Above 21.9 at% C, no indications of significant diffraction intensities can be observed.

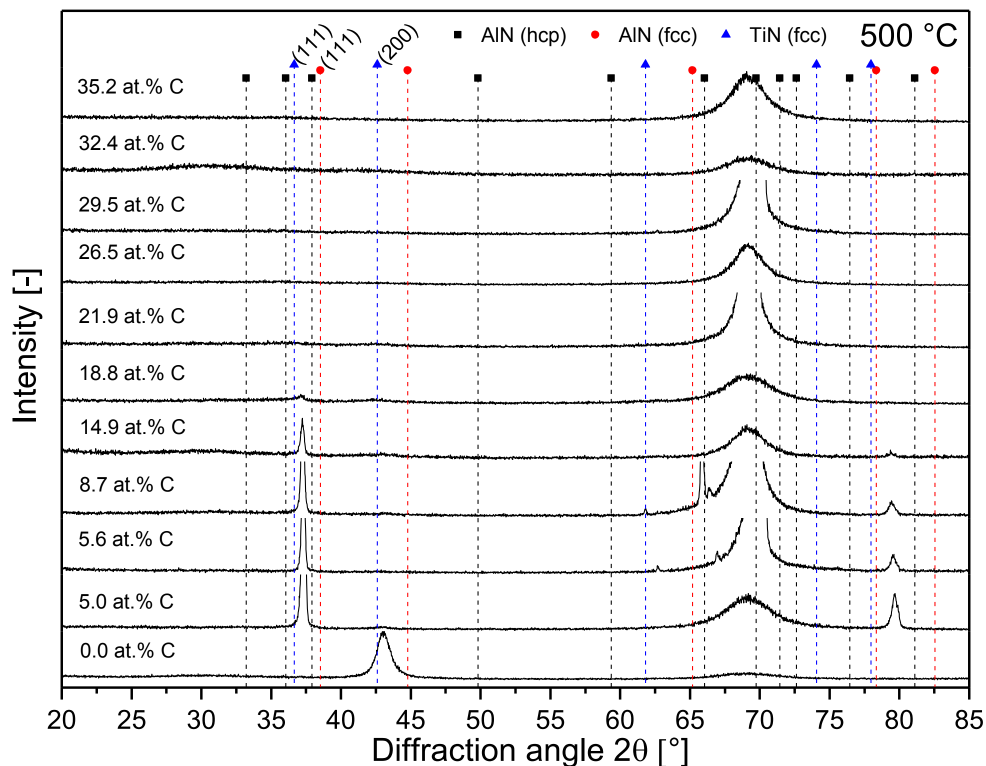

Figure 22 XRD patterns of TiAlNC coatings with various C contents deposited at 500 °C on Si (100) substrates.

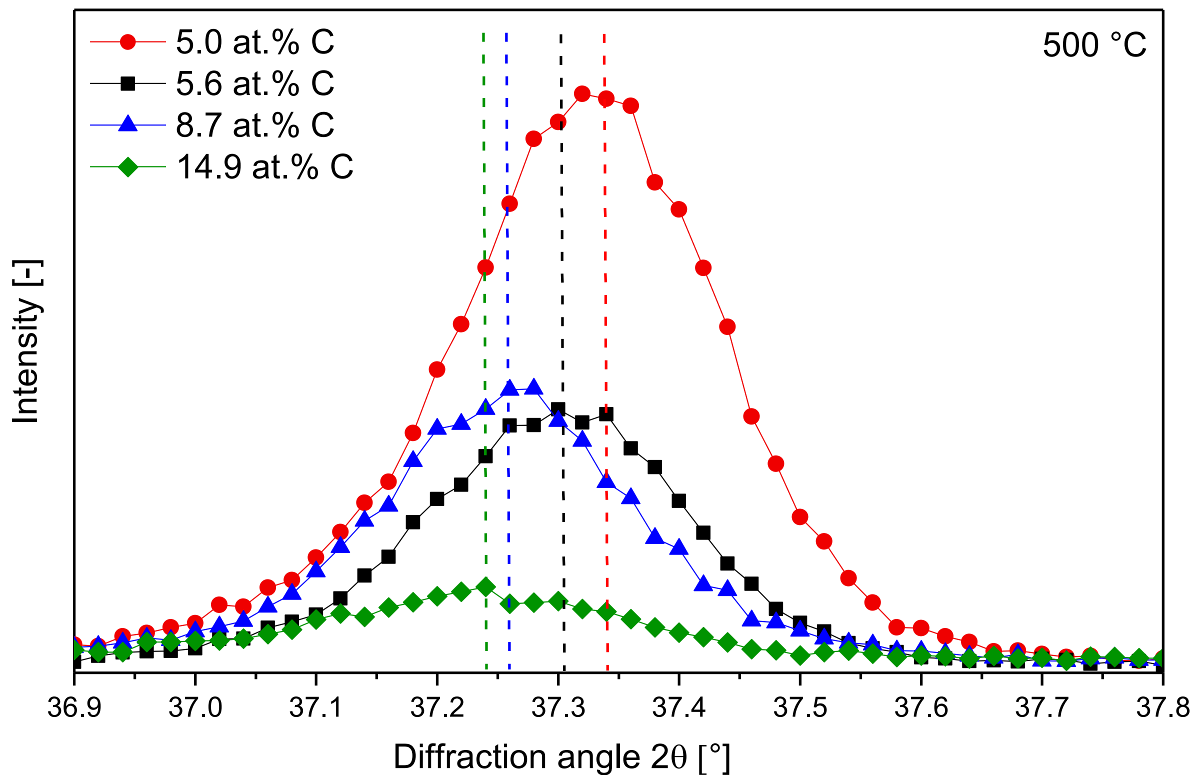

Figure 23 The shift of fcc-TiAlN (111) peak with increasing C content to lower diffraction angles. The vertical lines indicate the positions of the intensity maxima.

4.4 Raman Spectroscopy

Raman spectra of coatings deposited at 25 and 500 °C with different C contents are presented in Figure 24 and Figure 25. All spectra show different characteristics in the region between 1300 and 1600 cm^{-1}. If peaks occur in this region, they can be related to the so-called D and G bands and can be fitted using a convolution of Gaussian functions. In literature, the positions are given at 1360 for the D and 1560 cm^{-1} for the G band and are marked by vertical lines in the figure [31]. When the C content of the coatings deposited at 25 °C reaches 11.8 at.%, intensities corresponding to these overlapping D-G bands can be observed. A further increase of the C content leads to a significant increase of the D-G intensities. The coatings deposited at 500 °C also show increasing D-G band intensity with increasing C content.

However, D-G band intensities already appear at lower C contents (8.7 at.%) for the coatings deposited at 500 °C.

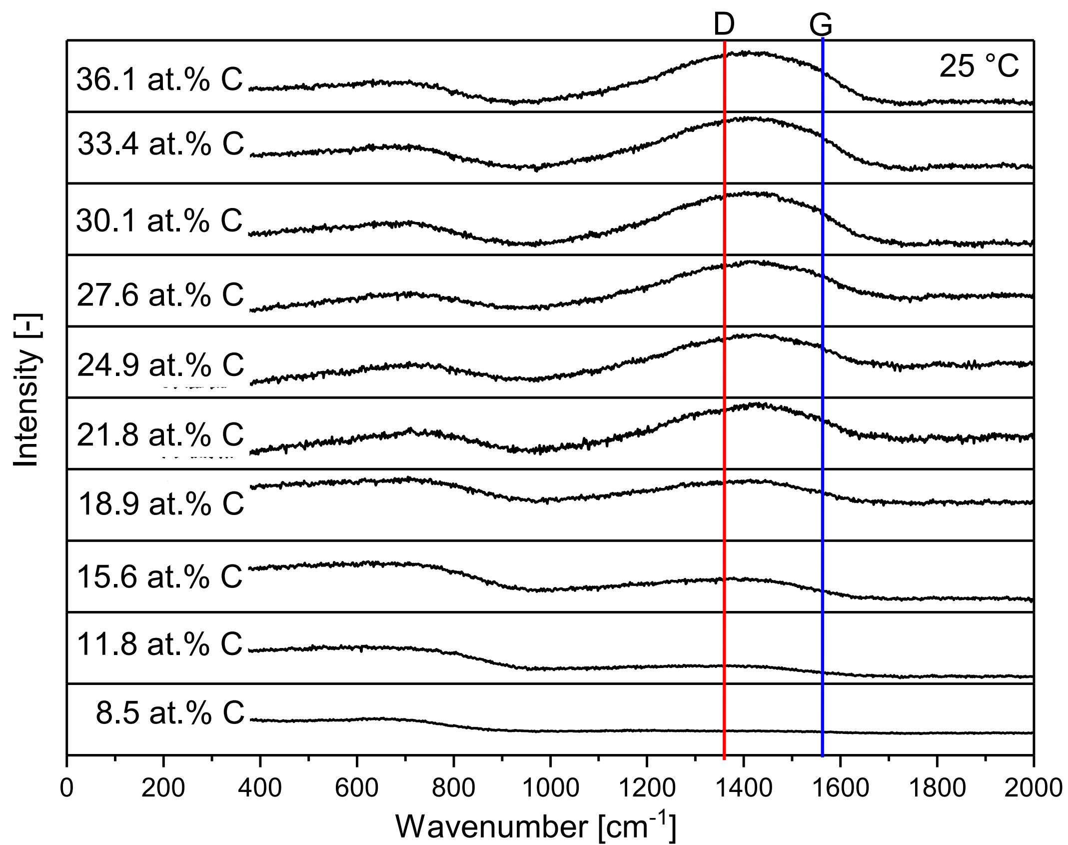

Figure 24 Raman spectra of the TiAlNC coatings deposited at 25 °C with various C contents.

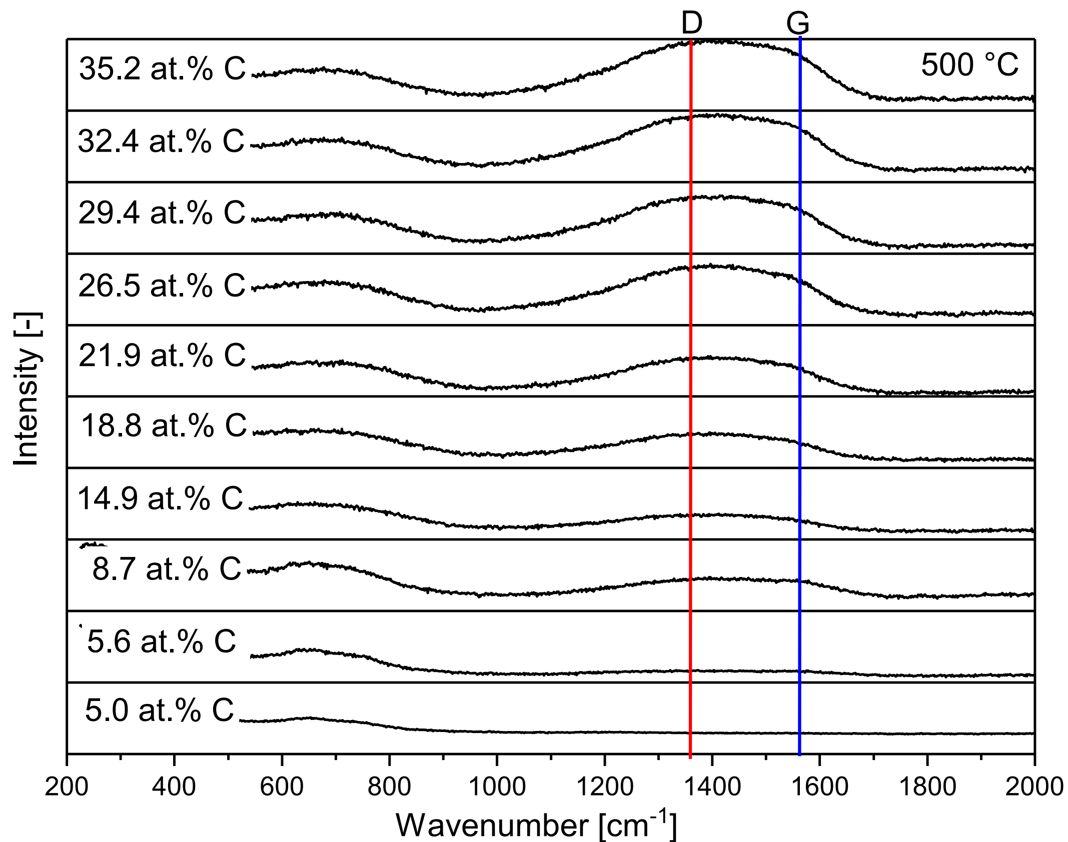

Figure 25 Raman spectra of the TiAlNC coatings deposited at 500 °C with various C contents.

Figure 26 demonstrates a detail of the D-G region of the Raman spectrum of a TiAlNC coating with a C content of 21.9 at.% deposited at 500 °C. The blue line in the diagram represents the cumulative fit of the measured spectrum, while the red dashed line represents the Gaussian fit of the G-peak and the green dashed-dotted line represents the Gaussian fit of the D-peak. An estimate of the I(D)/I(G) ratio was obtained by analysing the peak intensities.

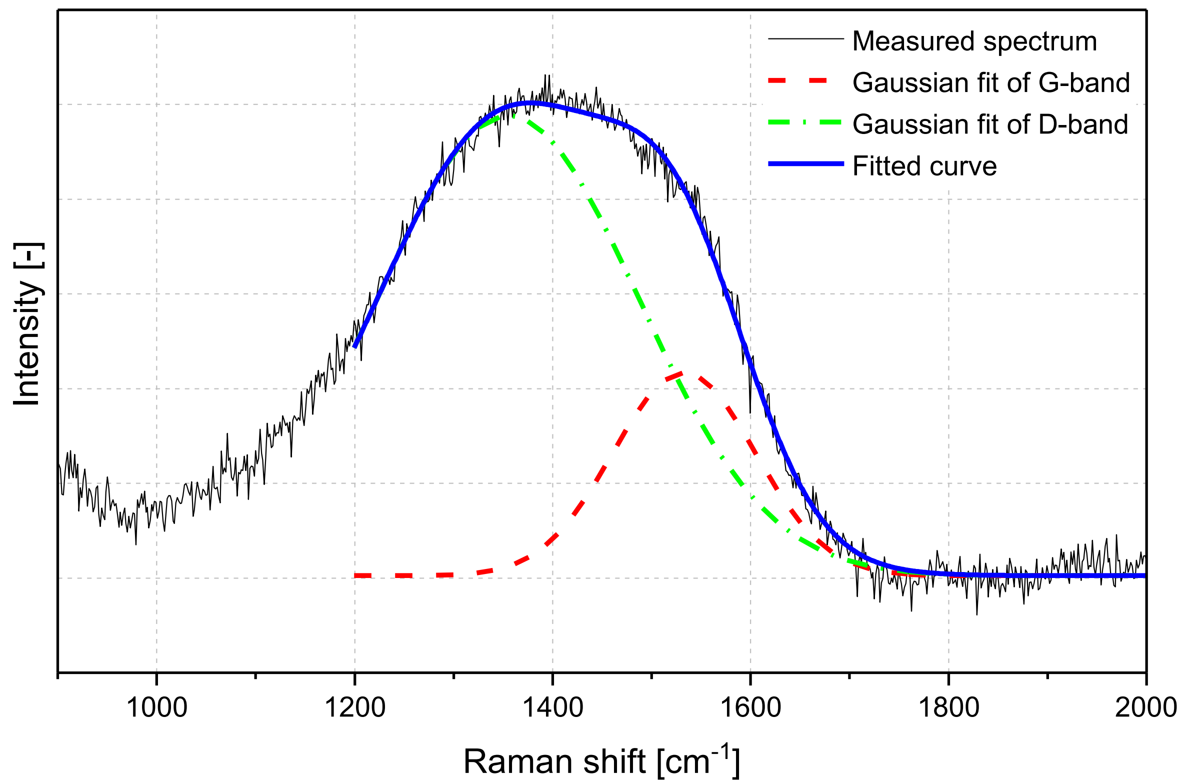

Figure 26 Raman spectrum detail of a measured TiAlNC coating with 21.9 at.% C deposited at 500 °C.

Figure 27 summarizes the I(D)/I(G) intensity ratio of the investigated coatings with respect to the C content. With increasing C content, the samples show an overall rise of the intensity ratio. The samples deposited at 25 °C show intensity ratios from 1.87 up to a maximum of 2.26, while the coatings deposited at 500 °C have a smaller I(D)/I(G) intensity ratio ranging from 1.28 up to a maximum of 2.09.

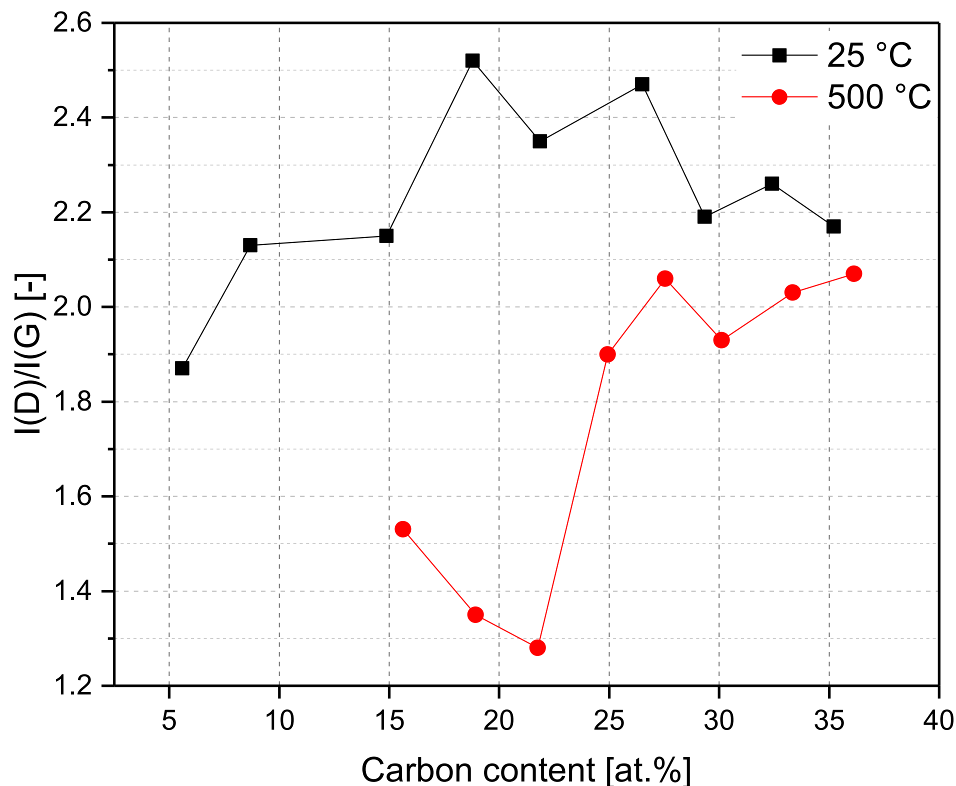

Figure 27 I(D)/I(G) ratio of the TiAlNC coatings deposited at 25 and 500 °C with various C contents.

4.5 X-Ray Photoelectron Spectroscopy

Figure 28 shows an exemplary XPS general survey scan performed on a TiAlNC coating with a C content of 14.9 at.% deposited at 500 °C. It provides information about the elements present in the coating. In this case Ti, Al, Ar, C, N and O were detected. Figure 29 shows the fitted XPS spectra for two coatings with a C content of 14.9 and 32.4 at.% deposited at 500°C. At a C content of 14.9 at.%, five bonding states were detected: the CO-O peak at 288.7, the C-O-C at 286.6, the C-C at 284.8, the C-TiN at 282.9 and the C-Ti peak at 281.95 eV (Figure 29a). With increasing C content, the C atoms exist mainly in two bonding states, which are the C-C and the C-TiN. Comparing Figure 29a and b, the C-C peak increases with increasing C content, whereas the C-Ti peak disappears.

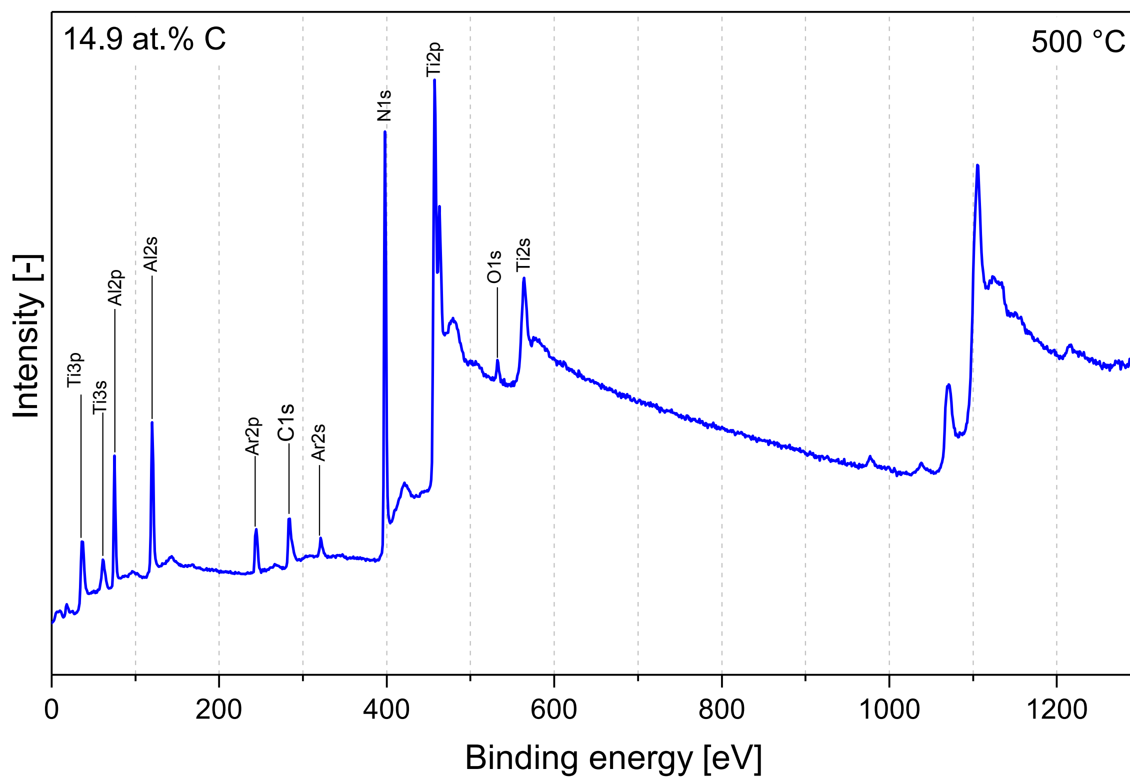

Figure 28 A representative XPS spectrum showing the occurring bonding states (14.9 at. % C deposited at 500°C).

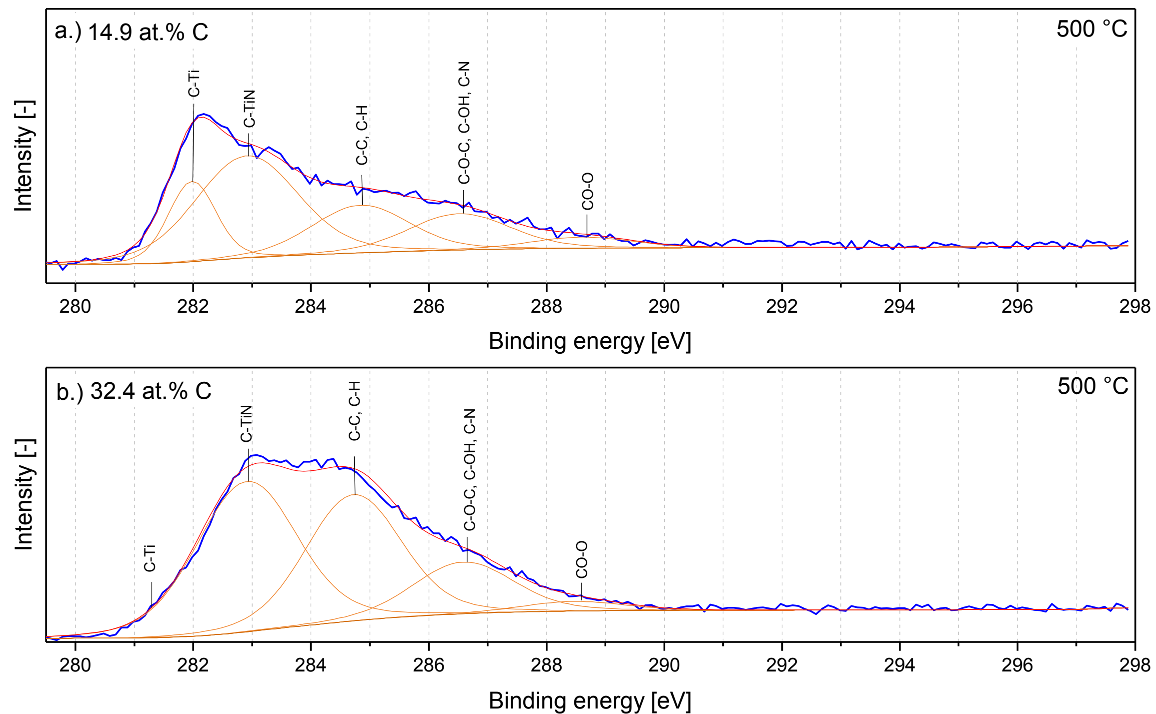

Figure 29 Fitted XPS spectra of the C1s peak deposited at 500°C with a C content of 14.9 at. % (a) and 32.4 at. % C (b).

4.6 Wafer Curvature Measurements

Figure 30 shows the residual stress values of coatings deposited at 25 and 500 °C. All analysed samples exhibit compressive stress except two samples of the 500 °C series. Both series show similar behaviour in terms of residual stress. The stress values of the 25 °C samples range from -1117 ± 55 to -263 ± 33 MPa and the residual stress of the coatings deposited at 500 °C range from -757 ± 55 to 77 ± 33 MPa. By increasing the C content, the compressive stress decreases from -1117 ± 55 MPa with 0.0 at.% C to -410 ± 34 MPa with 8.5 at.% C deposited at 25 °C and from -666 ± 45 MPa with 0.0 at.% C to 76.55 MPa with 5.0 at.% C deposited at 500 °C. By further increasing the C content, the compressive stress increases. After reaching a local maximum of -576 ± 30 MPa with 11.8 at.% C deposited at 25 °C and -757 ± 56 MPa with 18.8 at.% C deposited at 500 °C, the compressive stress continuously decreases again.

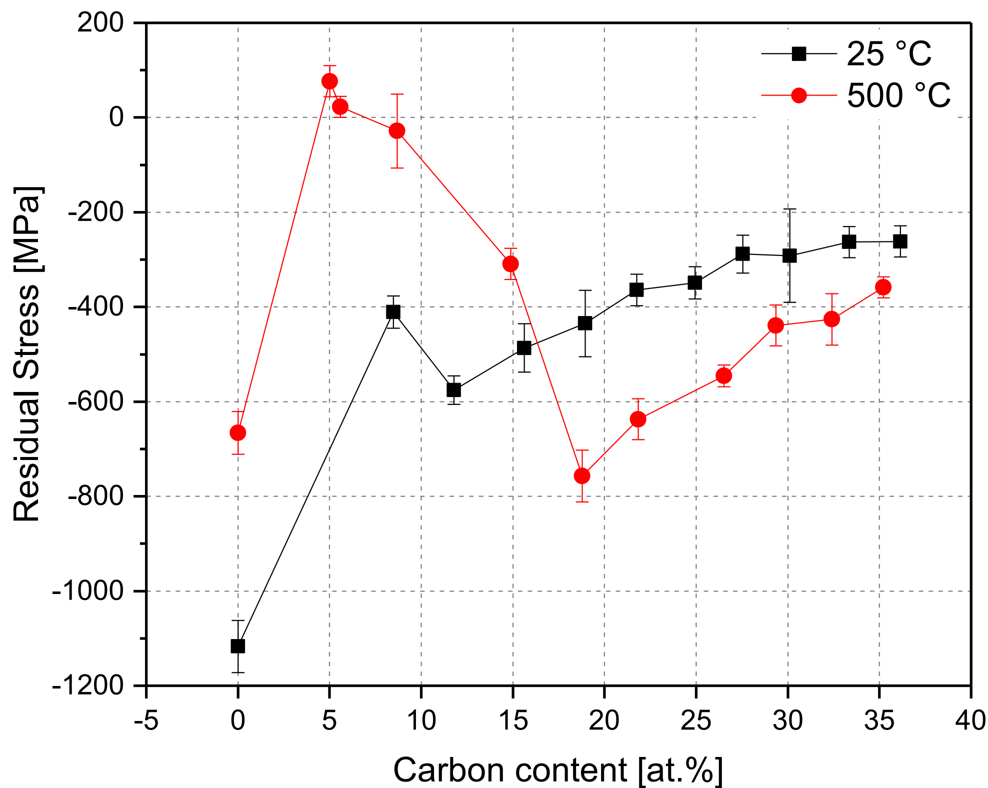

Figure 30 Residual stress of coatings deposited at 25 and 500 °C with different C contents.

4.7 Nanoindentation

The hardness and the elastic modulus of the coatings were determined by nanoindentation. The results obtained for the coatings with respect to the C content are displayed in Figure 31. Vertical error bars indicate the standard deviation of the measurements. Overall, the coatings show a decline of elastic modulus with increasing C content. The coating with 8.5 at.% C deposited at 25 °C exhibits the highest elastic modulus of 268.1 ± 9.3 GPa. The hardness of the TiAlNC coatings deposited at 25 °C increases and reaches the maximum hardness value of 19.5 ± 1.1 GPa when the C content is 18.9 at.%. With further increase of the C content, the hardness values decrease and reach 12.5 ± 0.6 GPa when the C content is 36.1 at.%. The coating deposited at 500 °C with the highest elastic modulus of 219.4 ± 7.6 GPa is found at 5.0 at.% C. With increasing C content, the hardness of the

coatings decreases from 19.2 ± 1.3 to 8.6 ± 0.2 GPa. The maximum hardness value is about 19.21 ± 1.3 GPa at the C content of 5.0 at.%.

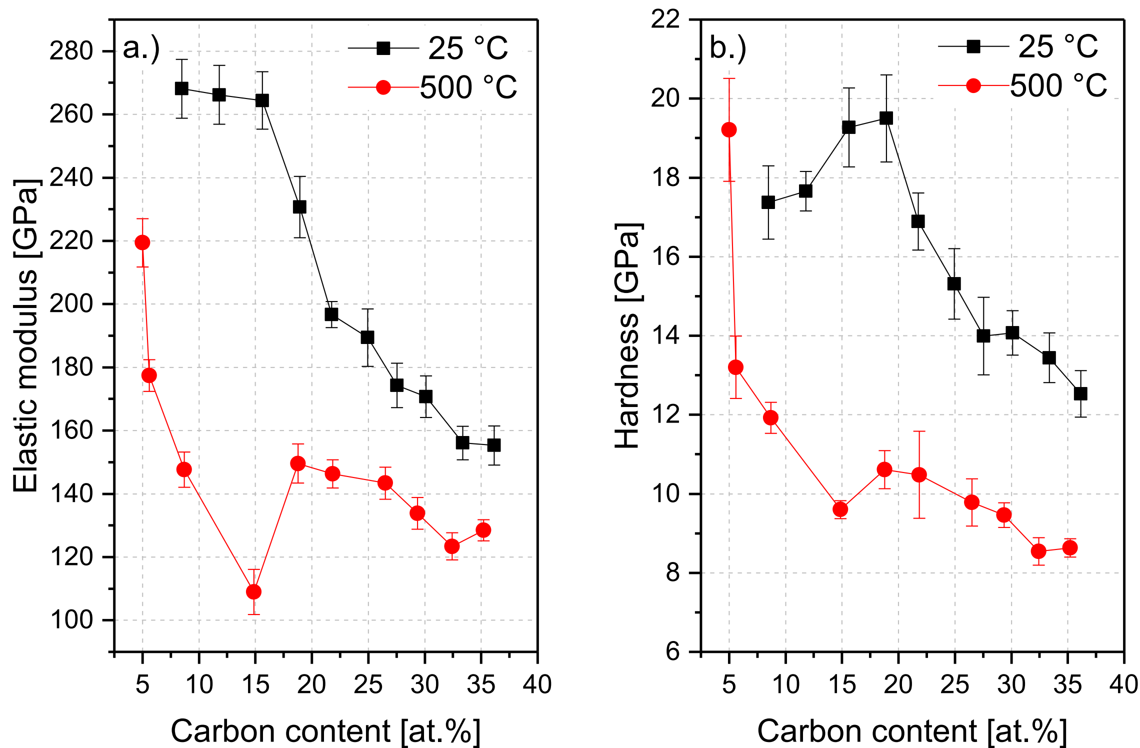

Figure 31 Elastic modulus (a) and hardness (b) of TiAlNC coatings with various C contents deposited at 25 °C and 500 °C. The thickness of C-free coatings was not sufficient for reliable nanoindentation measurements.

4.8 Four-Point Probe Measurements

The results of the sheet resistivity measurements on MgO substrates with respect to the C content are displayed in Figure 32. The electrical resistivity of the TiAlNC coatings deposited at 25 °C increases as the C content in the coatings increases and reaches the maximum electrical resistivity value of 132 Ωcm at 24.9 at.% C. With further increase of the C content, the resistivity values decrease and reach 40.3 Ωcm at a C content of 36.1 at.% (see Figure 32a). Figure 32b shows the electrical resistivity of the TiAlNC coatings deposited at 500 °C. All analysed samples exhibit electrical resistivity values between 0.01 and 0.62 Ωcm. Up to a C content of approximately 18.8 at.%,

the electrical resistivity remains below 0.5 Ωcm. With further increase of the C content, the electrical resistivity increases until a plateau of approximately 0.60 Ωcm is reached at 25.0 at.% C.

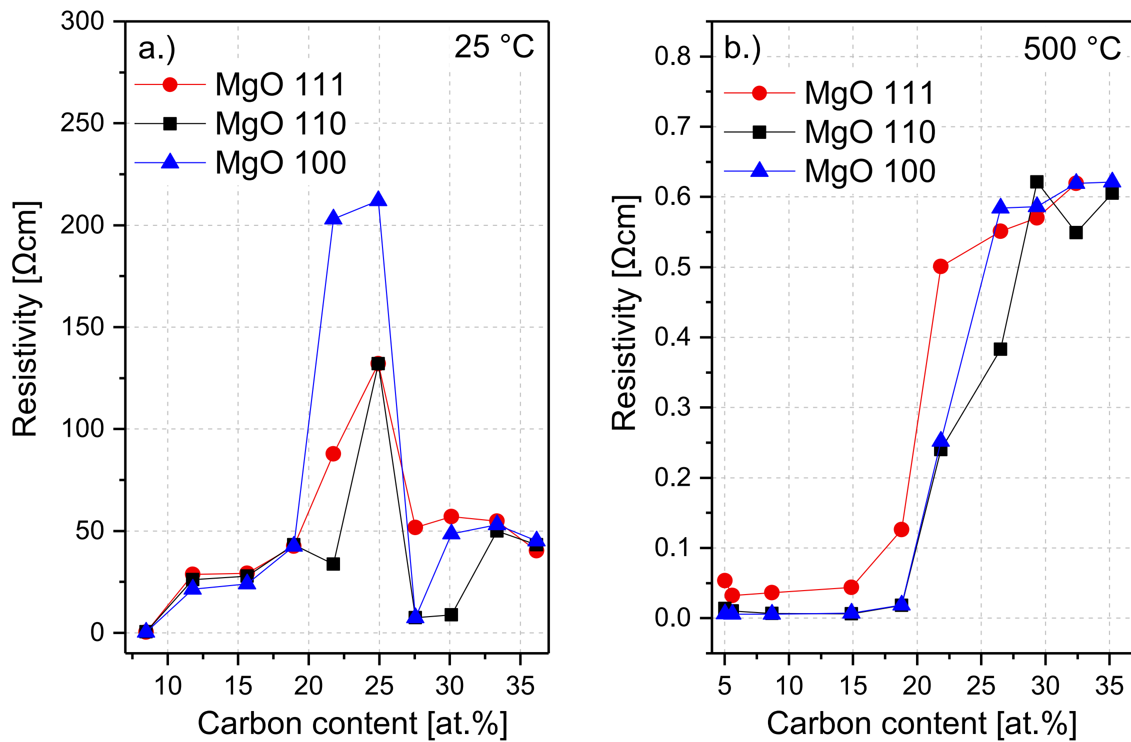

Figure 32 Electrical resistivity of TiAlNC coatings with various carbon content deposited at 25 °C (a) and 500 °C (b) onto MgO substrates with different orientations.

5 Discussion

By increasing the C target current during magnetron co-sputtering of Ti/Al and Cu targets from 0.02 to 0.2 A, the coating thickness and the C content in the coatings increase continuously (Table 4). Depending on the C content and the deposition temperature, crystalline or amorphous microstructures were observed. XRD patterns of TiAlNC coatings deposited at 25 °C with a C content up to 8.48 at.% indicated a crystalline structure (Figure 21), while formation of such a crystalline structure within TiAlNC coatings deposited at 500 °C is extended up to 14.88 at.% C (Figure 22). The presence of the crystalline structure indicates that the C atoms can be incorporated into the fcc-TiAlN lattice. Furthermore, a peak shift can be observed with increasing C content, which is attribtuted to an expansion of the fcc-TiAlN lattice (Figure 23). The expansion can be related to N atoms (single bond atomic radius: 72 pm) which are substituted by C atoms (single bond atomic radius: 77 pm) with a slightly larger atomic radius [41]. This is in accordance with the EDS results, which show a continuous decrease of the N content with increasing C content (Table 4). The good solubility of C in the fcc-TiAlN lattice can be attributed to the small differences in the atomic radii of C and N atoms [42]. The intercalation of the C atoms in the fcc-TiAlN lattice can also be explained by the residual stress evolution (Figure 30). As the C content increases, a rise in the compressive stress can be observed. This could result from the mentioned replacement of N by slightly larger C atoms via a substitional mechanism. However, if the C content exceeds the solubility limit of the fcc-TiAlN lattice, which seems to be above 8.48 at.% and 14.88 at.% for coatings deposited at 25 and 500 °C, respectively, a decrease of the compressive stress can be observed. As shown in Figure 23, a broadening of the (111) peaks with increasing C content was observed, which demonstrates the reduction of the domain sizes of the coatings. As evidenced by Raman spectroscopy, an amorphous C phase is formed. The intensities corresponding to the overlapping D-G bands increase with increase of the carbon content, which indicates the existence of an a-C phase at higher C contents [43]. Due to the increase of the intensities it can be assumed that the amount of a-C is

proportional to the C content in the coating. In this structure, excess C atoms can precipitate at the TiAlN grain boundaries as a-C and a relaxation of the lattice takes place, as previously reported by Zeng et al. [44]. Additional information of the C bonding states was obtained from XPS measurements (Figure 26). At higher C contents (32.41 at. %), C atoms mainly exist in two bonding states, which are C-C at 284.8 eV and C-TiN at 282.9 eV, demonstrating that an amorphous TiAlNC structure with a-C precipations exists, since no crystalline phase is evident by XRD.

The results of the nanoindentation measurements point out the influence of the C content on the mechanical properties of TiAlNC coatings. Coatings deposited at 25°C with low C contents show the highest hardness and elastic modulus values, which can be related to solid solution hardening of the fcc-TiAlN lattice by C atoms. Another reason for improving the hardness at lower C contents is the reduced grain size caused by C incorporation, which hinders dislocation movement [45]. After reaching a maximum, a further increase of the C content leads to the reduction of the hardness and the elastic modulus, which can be related to the precipitation of a soft a-C phase at grain boundaries. The coatings exhibit a maximum hardness of 19.5 ± 1.1 GPa and a maximum elastic modulus of 268 ± 9 GPa, which is lower than comparable TiAlNC coatings [44,46].

The electrical properties of TiAlNC coatings depend on the C content and the deposition temperature, as can be seen in Figure 32. The increase of the electrical resistivity with increasing C content can be explained by serveral factors. On the one hand, C incorporation leads to grain refinement, which increases the number of grain boundaries. The grain boundaries act like electrical potential barriers, which reduce the charge carrier transport and therefore result in an increased electrical resistivity [47]. On the other hand, the increase of the resistivity can be explained by the sp^3/sp^2 ratio evolution. As shown in Figure 27, the amount of the electrically conductive sp^2 phase decreases with increasing C content, which contributes to the observed increase of the electrical resitivity. Coatings deposited at 25 °C yield higher resitivity values compared to coatings deposited at 500 °C. This could be

explained by the increased grain growth due to enhanced diffusion processes at elevated temperatures.

6 Conclusion

The aim of this study was to investigate the structural, mechanical and electrical effects of C alloyed to sputtered TiAlN coatings. Therefore, TiAlNC coatings with various C contents were deposited on Si and MgO substrates by magnetron co-sputtering from Ti/Al and C targets at 25 and 500 °C. By continuously increasing the current on the C target, TiAlNC coatings with C contents up to 36.1 and up to 35.2 at.% C at 25 and 500 °C, respectively, were synthesized. The microstructure of the coatings was characterized using X-ray diffraction and Raman spectroscopy, which revealed that with increasing C content the microstructure changes from crystalline TiAlN to amorphous TiAlNC. At lower C contents, the microstructure consisted of crystalline TiAlNC grains, in which the C atoms replace the N atoms via a substitional mechanism. With increasing C content, a reduction of the domain sizes was observed and finally an amorphous TiAlNC phase with amorphous C precipitations at grain boundaries is formed. A maximum hardness value obtained by nanoindentation of 19.5 ± 1.1 GPa was found, when the C content reached 18.9 at.% and the deposition temperature was 25 °C, which could be related to solid solution hardening and a refined grain structure. The investigations of the electrical properties indicated that the resistivity increases with rising C content, which could be related to the grain refined structure at higer C contents and a higher sp^3/sp^2 ratio. The results obtained within this thesis facilitate the optimization of composition and deposition conditions in order to develop a new generation of hard coatings.

7 References

[1] S. PalDey, S.C. Deevi, Single layer and multilayer wear resistant coatings of (Ti,Al)N: A review, Mater. Sci. Eng. A. 342 (2003) 58–79. doi:10.1016/S0921-5093(02)00259-9.

[2] K. Kutschej, P.H. Mayrhofer, M. Kathrein, P. Polcik, C. Mitterer, Influence of oxide phase formation on the tribological behaviour of Ti–Al–V–N coatings, Surf. Coatings Technol. 200 (2005) 1731–1737. doi:10.1016/j.surfcoat.2005.08.044.

[3] X. Zhang, J. Jiang, Z. Yuqiao, J. Lin, F. Wang, J.J. Moore, Effect of carbon on TiAlCN coatings deposited by reactive magnetron sputtering, Surf. Coatings Technol. 203 (2008) 594–597. doi:10.1016/j.surfcoat.2008.06.175.

[4] D.M. Mattox, Handbook of Physical Vapor Deposition (PVD): Film Formation, Adhesion, Surface Preparation and Contamination Control, Noyes Publications, New Jersey, 1998. doi:10.1080/10426919908907566.

[5] F.-W. Bach, A. Laarmann, T. Wenz, C.B. Nakhosteen, Modern Surface Technology, ,Wiley-VCH, Weinheim, 2006.

[6] S.A.M. Al-Bat'hi, Electrodeposition of Nanostructure Materials, in: M. Aliofkhazraei (ed.), Electroplating of Nanostructures, InTech, Malaysia, 2015. doi:10.5772/61389.

[7] P.M. Martin, Handbook of Deposition Technologies for Films and Coatings: Science, Applications and Technology., Elsevier Science, Burlington, 2009.

[8] R.A. Haefer, Oberflächen- und Dünnschicht-Technologie Teil I: Beschichtungen von Oberflächen, Springer, Berlin Heidelberg, 1987.

[9] C. Mitterer, PVD and CVD Hard Coatings, in: V.K. Sarin (Editor-in-Chief), L. Llanes, D. Mari (Vol. Eds.) Comprehensive Hard Materials), Vol. 2, Elsevier, Amsterdam, 2014, 449–467. doi:10.1016/B978-0-08-096527-7.00035-0.

[10] M. Ohring, Materials Science of Thin Films: Deposition and Structure, Academic Press, San Diego, 2002.

[11] G. Kienel, Vakuum-Beschichtung 4 - Anwendungen Teil 1, VDI-Verlag, Berlin, 1993.

[12] M.A. Lieberman, A.J. Lichtenberg, Principles of Plasma Discharges and Materials Processing, Wiley-Interscience, New York, 2005.

[13] A.A. Fridman, Plasma Chemistry, Cambridge University Press, Cambridge, 2008.

[14] Z.H. Barber, The control of thin film deposition and recent developments in oxide film growth, J. Mater. Chem. 16 (2006) 334–344. doi:10.1039/B506228D.

[15] H. Luth, Solid Surfaces, Interfaces and Thin Films, Springer, Berlin, 2014.

[16] Y. Pauleau, P.B. Barna, Protective Coatings and Thin Films: Synthesis, Characterization and Applications, Springer, London, 1997.

[17] B.A. Movchan, A.V. Demchishin, Investigations of the structure and properties of thick Ni, Ti, W, Al_2O_3 and ZrO_2 vacuum condensates, Fiz. Met. Met. 28 (1969) 653-660.

[18] J.A. Thornton, Influence of apparatus geometry and deposition conditions on the structure and topography of thick sputtered coatings, J. Vac. Sci. Technol. 11 (1974) 666–670. doi:10.1116/1.1312732.

[19] R. Messier, A.P. Giri, R.A. Roy, Revised structure zone model for thin film physical structure, J. Vac. Sci. Technol. A Vacuum, Surfaces and Films. 2 (1984) 500–503. doi:10.1116/1.572604.

[20] P. Barna, M. Adamik, Growth mechanisms of polycrystalline thin films, in F.C. Matacotta, G. Ottaviani (eds.), Science and Technology Thin Films, World Scientific, Singapore,1995, 1–28.

[21] H.A. Jehn, S. Hofmann, V. Rückborn, W. Münz, Morphology and properties of sputtered (Ti,Al)N layers on high speed steel substrates as a function of deposition temperature and sputtering atmosphere, J. Vac. Sci. Technol. 4 (1986) 2701–2705. doi:10.1116/1.573709.

[22] W. Münz, Titanium aluminum nitride films: A new alternative to TiN coatings, J. Vac. Sci. Technol. 4 (1986) 2717–2725. doi:10.1116/1.573713.

[23] C.W. Kim, K.H. Kim, Anti-oxidation properties of TiAlN film prepared by plasma-assisted chemical vapor deposition and roles of Al, Thin Solid Films. 307 (1997) 113–119. doi:10.1016/S0040-6090(97)00212-5.

[24] B.-J. Kim, Y.-C. Kim, J.-W. Nah, J.-J. Lee, High temperature oxidation of $(Ti_{1-X}Al_X)N$ coatings made by plasma enhanced chemical vapor deposition, J. Vac. Sci. Technol. 17 (1999) 133–137. doi:10.1116/1.581562.

[25] J.C. Schuster, J. Bauer, The ternary system titanium-aluminum-nitrogen, J. Solid State Chem. 53 (1984) 260–265. doi:10.1016/0022-4596(84)90100-2.

[26] H. Holleck, Metastable coatings — Prediction of composition and structure, Surf. Coatings Technol. 36 (1988) 151–159. doi:10.1016/0257-8972(88)90145-4.

[27] M. Kawate, A. Kimura, T. Suzuki, Microhardness and lattice parameter of $Cr_{1-x}Al_xN$ films, J. Vac. Sci. Technol. A Vacuum, Surfaces and Films. 20 (2002) 569–571. doi:10.1116/1.1448510.

[28] J.G. Han, J.S. Yoon, H.J. Kim, K. Song, High temperature wear resistance of (TiAl)N films synthesized by cathodic arc plasma deposition, Surf. Coatings Technol. 86–87 (1996) 82–87. doi:10.1016/S0257-8972(96)02964-7.

[29] M. Zhou, Y. Makino, M. Nose, K. Nogi, Phase transition and properties of Ti–Al–N thin films prepared by r.f.-plasma assisted magnetron sputtering, Thin Solid Films 339 (1999) 203–208. doi:10.1016/S0040-6090(98)01364-9.

[30] P.H. Mayrhofer, A. Hörling, L. Karlsson, J. Sjölén, T. Larsson, C. Mitterer, L. Hultman, Self-organized nanostructures in the Ti–Al–N system, Appl. Phys. Lett. 83 (2003) 2049–2051. doi:10.1063/1.1608464.

[31] J. Robertson, Diamond-like amorphous carbon, Mater. Sci. Eng. R Reports. 37 (2002) 129–281. doi:10.1016/S0927-796X(02)00005-0.

[32] M.H. Nazaré, A.J. Neves, Properties, Growth and Applications of Diamond, Institution of Electrical Engineers, London, 2001.

[33] P.H. Mayrhofer, Materials science aspects of nanocrystalline PVD hard coatings, ph.d. thesis, Montanuniversität Leoben, 2001.

[34] K. Nitzsche, Schichtmesstechnik, Vogel Buchverlag, Würzburg, 1997.

[35] H. Zeman, J. Musil, J. Vlček, P.H. Mayrhofer, C. Mitterer, Thermal annealing of sputtered Al–Si–Cu–N films, Vacuum. 72 (2003) 21–28. doi:10.1016/S0042-207X(03)00094-0.

[36] D. Winkler, Konzeption und Realisierung thermisch unterstützten Meßverfahrens zur Bestimmung von Eigenspannungen in dünnen Schichten, Diplomarbeit, Montanuniversität Leoben, 1997.

[37] R. Daniel, K.J. Martinschitz, J. Keckes, C. Mitterer, The origin of stresses in magnetron-sputtered thin films with zone T structures, Acta Mater. 58 (2010) 2621–2633. doi:10.1016/j.actamat.2009.12.048.

[38] G.G. Stoney, The tension of metallic films deposited by electrolysis, Proc. R. Soc. A Math. Phys. Eng. Sci. 82 (1909) 172–175. doi:10.1098/rspa.1909.0021.

[39] W.C. Oliver, G.M. Pharr, An improved technique for determining hardness and elastic modulus using load and displacement sensing indentation experiments, J. Mater. Res. 7 (1992) 1564–1583. doi:10.1557/JMR.1992.1564.

[40] J. Chan, P. Friedberg, Four-Point Probe Manual, The University of California, Berkeley, 2002.

[41] P. Paetzold, Chemie: eine Einführung, Walter de Gruyter, Berlin, 2009.

[42] F.A. Cotton, G. Wilkinson, P.L. Gaus, Basic Inorganic Chemistry, J. Wiley, New York, 1995.

[43] Y.Z. Huang, M. Stueber, P. Hovsepian, The significance of carbon on the microstructure of TiAlNC coatings deposited by reactive magnetron sputtering, Appl. Surf. Sci. 253 (2006) 2470–2473. doi:10.1016/j.apsusc.2006.05.003.

[44] Y. Zeng, Y. Qiu, X. Mao, S. Tan, Z. Tan, X. Zhang, J. Chen, J. Jiang, Superhard TiAlCN coatings prepared by radio frequency magnetron sputtering, Thin Solid Films. 584 (2015) 283–288. doi:10.1016/j.tsf.2015.02.068.

[45] Y. Wang, L. Zhengxian, D. Jihong, H. Yunfeng, W. Baoyun, (Ti,Al,Si,C)N nanocomposite coatings synthesized by plasma-enhanced magnetron sputtering, Appl. Surf. Sci. 258 (2011) 456–460. doi:10.1016/j.apsusc.2011.08.094.

[46] X. Zhang, Y. Qiu, Z. Tan, J. Lin, A. Xu, Y. Zeng, J.J. Moore, J. Jiang, Effect of Al content on structure and properties of TiAlCN coatings prepared by magnetron sputtering, J. Alloys Compd. 617 (2014) 81–85. doi:10.1016/j.jallcom.2014.08.009.

[47] P. Wellmann, Materialien der Elektronik und Energietechnik Halbleiter, Graphen, Funktionale Materialien, Springer Vieweg, Nürnberg, 2017.